Master Thesis

Erasmus Mundus Master in Decentralized Smart Energy Systems, with Thermal Energy Specialization

Parametric Study of Thermal-Large Eddy Simulation (T-LES) Models in Turbulent Anisothermal Channel Flow

Report

Author: Srijan Dasgupta
Director: Carlos David Perez Segarra
Supervisor: Adrien Toutant, Lionel Mathelin, Yanis Zatout

Call: July 2023

Higher Technical School
of Industrial Engineering from Barcelona

Abstract

Thermal Large eddy simulations (T-LES) are getting more and more popular becuase of the availability of computational power in the industries, thus the necessity of testing out different T-LES models are necessary. This thesis assesses two different types of thermal large eddy simulation models. This study was done for highly anisothermal flow for pressurized air as the fluid in the channel flow of a solar receiver of a tower of concentrated solar power (CSP) plant. The study was done to compare the results of the two chosen T-LES models and how they compare with the DNS data of similar settings. For this purpose, both T-LES models were simulated with similar thermal conditions, heat fluxes and mesh configurations. The mean value of the friction Reynolds number was around 800 for all simulations. In terms of solving the Navier-stokes, the equations were simplied using low-Mach number assumption. Due to the filtering operation of the LES method, two major non-linear unclosed sub-grid terms for velocity-velocity and velocity-density correlations appears that has a signficant affect on the flow characteristics, thus these terms need to be modeled. There are two types of models called functional and structural models. However, one functional and two-layererd mixed model that mixes both functional and structural models has been investigated with fourth order discretization scheme on the momentum conservation equation and 2nd order scheme on the mass conservation equation for both cases. After simulating the T-LES configurations, the errors were calculated for the mean and correlation quantites by comparing them with the DNS data to check the accuracy of each model. Also, normalized profiles were generated and assesed as a function of the distance from the wall.

Content _

Glossary and Nomenclature

Abbreviations

CFD: Computationa Fluid Dynamics

LES: Large Eddy Simulation

CSP: Centralized Solar Power

RANS: Reynolds Average Navier Stokes

DNS: Direct Numerical Simulations

N-S: Navier Stokes

CFL: Caurant Friedrichs-Lewy

SGS: Sub-Grid Scale

AMD: Anisotropic Minimum Dissipation

Symbols

a: Mesh dilation parameter

T : Absolute temperature (K)

C_p : Constant pressure heat capacity ($Jkg^{-1} \cdot K^{-1}$)

C_v : Constant volume heat capacity ($Jkg^{-1} \cdot K^{-1}$)

N: Number of grid points

Re: Reynolds numver (dimensionless)

k: Wave number

g: Velocity gradient (s^{-1})

d: Scalar gradient

Ma= Mach number

Pr= Prandtl number

C= Velocity of sound (ms^{-1})

P: Mechanical pressure (Pa)

P_0: Thermodynamic pressure (Pa)

Q: Conduction heat flux (W/m^3)

Re_τ: Friction Reynolds number (dimensionless)

r: Ideal specific gas constant (J/kg/K)

t: time (s)

S: Strain rate tensor (s^{-1})

U: Velocity vector (m/s)

U_τ: Friction velocity vector (m/s)

x, y, z: Cartesian coordinates

α: Constant pressure coefficient of thermal expansion (K^{-1})

β: Constant volume coefficient of thermal expansion (K^{-1})

μ: Dynamic viscosity (Pa.s)

v: Kinematic viscosity (m^2/s)

λ: Thermal conductivity (W/m/K)

ρ: Density (kg/m^3)

τ: Velocity-velocity subgrid term

π: Velocity-density subgrid term

Σ: Viscous stress tensor (Pa)

Υ: Total stress tensor (Pa)

List of figures

List of tables

1. Introduction

The energy crisis is one of the most significant problems, if not the most significant problem the world is currently facing in the present time. This energy crisis is not just attributed due to the steady depletion of the current known fossil fuel reserves, it is also due to the effects on the climate which is already noticeable due to the major dependence on fossil fuel technologies so far. Therefore, the dependency on fossil fuels should be severely cut down not only to decelerate the depletion of the fossil fuel reserves, but also to prevent the climate emergency we are bound to face due to the green-house gas emissions associated with the fossil fuel usage. And as the world is focusing on the transition of energy technologies to more sustainable and climate friendly options, the role of solar and wind energy in this regard is the most significant in terms of renewable sources of energy[1]. Out of different options, hydroelectricity is a very good solution because of the capacity of storage, however it has the limitation of geographical locations. As most of the location that are favorable for hydroelectricity are already occupied with plants, the room for further progress for this renewable option is slim[2]. Although solar photovoltaics and wind energy are quite established compared to the other renewable energy technologies for power generation, these technologies produce electricity directly, which poses the question of storage as well.

Concentrated solar power (CSP) plants has a lot of potential in the future in terms of establishing more plants, having technical availability and having storage opportunities of energy as high temperature heat, unlike solar photovoltaics [3]. This high temperature heat storage capacity of CSP plants can help it integrate with a lot of technologies and can be utilized for different kinds of applications [4][5]. In CSP plants, concentrators are used to concentrate the solar radiation on the top of a central tower receiver, where the heat is transferred to a heat carrying fluid to later utilize the heat energy for different purposes. In the current CSP plants, molten salts are used mostly in the receiver as the heat carrying fluid. However, molted salt temperature has its own limitations, one of them is having a maximum reaching temperature value of 950K in recent technologies[5][6]. The new generation CSP plants are in research phase to increase the maximum temperature, and different fluids like particles[7], mixture of fluid and particles[8], liquid metals[9] and pressurized gas[10] are being investigated. There are several advantages of using pressurized air for CSP plants. First, there is an abundance of air everywhere, whereas fluids like molten salts have to be carried to the plant site for usage. The environmental effects of other fluids are an issue, whereas for air there is no such concern. Most importantly, the pressurized air temperature can cross the maximum temperature limit of the molten salt and reach up to 1200K, which will increase the efficiency of the thermodynamic cycle of the system, as well as this high temperature can be utilized to run cycles like Brayton cycles for power generation [4].

In this thesis, the focus of our investigation is pressurized air as the CSP plant receiver heat carrying fluid and performing CFD simulations, more specifically LES method to better

understand the physics behind the solar receiver channel flow of pressurized air so that the thermal transfer between the receiver wall and the heat carrying fluid can be maximized while also focusing on minimizing the pressure losses.

1.1. Motivation

This thesis is essentially a part of the SOLAIRE ANR project in collaboration with PROMES-CNRS and LISN-CNRS lab. The major focus of the project is to enhance the efficiency of the conversion of solar energy into usable energy to produce electricity. The motivation of the work of the thesis is to evaluate different LES sub-grid scale models on different meshes and under various physical conditions to ensure accurate assessments. It is quite essential to have better understanding of different Thermal Large Eddy Simulations (T-LES) models as performing DNS method is quite expensive and difficult for complex geometries. Although T-LES models are quicker, much cheaper and reliable in most cases, but it lacks accuracy due to the extreme conditions of the pressurized air solar receivers. To calculate the sub-grid scales accurately, understand the effects of different models on the simulation results and to improve upon the models so that we can rely on T-LES models, different sub-grid models have to be investigated.

1.2. Objectives of the work

The particular objectives of the work were:

- Bibliographic study of the procedures of performing LES sub-grid model simulations.
- Bibliographic study of the different LES sub-grid models of interest and their influence on the statistics of the simulation.
- To choose and simulate one of the already performed test cases by one of the bibliographies.
- To choose different configurations of T-LES models to perform the test on them and compare the data with the DNS data.
- To compare the results between functional and mixed models and how they influence the results.
- To understand the effects of the meshes, discretization schemes and thermal conditions on the accuracy of the simulation results.

2. Literature review

For the solar receivers using pressurized air as the channel flow heat carrying fluid, the thermal conditions are really extreme, which results in highly anisothermal, asymmetrical heating with great turbulence [10]. To assess the performance of different conditions of the solar receiver in terms of the heat transfer between the heat carrying fluid and the receiver wall, numerical simulations are required as Navier-stokes equations does not have analytical solution for problems as complex as our case [11]. However, the solar receiver size, along with the flow characteristics can cause a lot of computational cost if the DNS method is used for investigating the channel flow, as DNS method tries to resolve all the smallest scales down to the Kolmogorov's scales. In terms of the LES method, this cost can be reduced down by a large factor, as the principal method of LES is to resolve the larger scales of the turbulence, and the unresolved sub-grid terms can be modeled using several LES sub-grid models. As the computational cost is much lesser than the DNS, this LES methodology can also be used for cases with complex geometry and extreme thermal conditions as well to better understand the heat transfer phenomenon between the receiver wall and the heat carrying fluid [12]. Different studies have been done regarding the study of complex anisotropic and asymmetrical flows for high temperature applications. It was seen in the study performed by Rayleigh-Taylor and Richtmyer-Meshkov that high temperature applications involves taking into account the velocity-temperature correlation term due to the high gradient of temperature[13][14]. An investigation by Peng and Davidson [15] presents a proposal of solving the heat flux of the sub-grid scale by using the strain rate tensor and the high gradient of temperature of the large scales. However, the local under-dissipation of this model sometimes even showcased negative value of the dissipation, which causes instability and simulation blow-up, which concludes that this SGS model for heat flux cannot be used on its own. To address this issue, an SGS heat flux mixed model was later proposed by Higgins et al. [16] by using models of Smagorinsky[17] and Leonard [18]. Unlike the study done by Peng and Davidson, another alternative approach to determine the sub-grid term heat flux was proposed by Wang et al. [19], where the sub-grid heat flux models were constructed using the sub-grid tensor of stress and the temperature gradient of the resolved scales.

Till now, the calculation of the heat flux has been performed using constant value of the Prandtl number models for turbulent flows. The unresolved eddy-diffusivity term from the energy equation of the Navier stokes equations were investigated by Wong and Lilly [20], where they calculated the unresolved velocity-temperature sub-grid term with temperature gradient while reducing the computational time and achieving good agreement with DNS values. In this study, the scaling formulation utilized the analysis of the Kolmogorov scale and computed the heat flux for the sub-grid scales using filter grid width and rate of dissipation.

There were several previous studies, that explored the possibility of introducing two-layered

mixed models for flow conditions with isothermal characteristics in order to get better simulation performance and results[21][22][23]. One of the most significant models was also proposed by Streher et al. [24], where they proposed that near wall turbulence can be modeled using both functional and structural models due to high value of viscous stresses, whereas only structural models should be considered away from the all due to the high influence of turbulent stresses near that region. Recent studies has also been performed for anisothermal channel flows to understand the effects of the turbulent temperature gradients, such as the effects of variable values viscosity and thermal conductivity on the heat transfer of turbulent flow performed by Wang et al [19]. Finally, Martin and Adrien et al. [12] have performed several investigations of different combinations of one and two layered mixed models for anisothermal channel flows in a solar receiver for pressurized air for multiple extreme thermal operating conditions at high temperature gradients to assess the performance, accuracy and reliability of different T-LES models with respect to the DNS data at similar operating conditions.

3. Methodology

3.1. Case definition

The gas pressurized solar receiver is a complex system with highly anisotropic behavior and asymmetric heating. The flow is highly turbulent, and the temperature is extremely high due to the concentrated solar energy as well. To study the configuration of the solar receiver for performing the parametric study of different LES models, the channel height is taken as 3mm. The channel configuration and the flow direction relative to the coordinates can be seen in **figure 3.1**. According to the direction, it can be noted that the x direction is the direction of the fluid stream, thus x denotes the streamwise direction of the system. The y direction is perpendicular to the hot and the cold wall, thus the y direction is the wall normal direction. Finally, the z direction is the spanwise direction. The wall temperatures are considered as being constant throughout time and space, although for real cases it is not homogeneous. Also, the boundary conditions for thermal properties are not constant as well. Usually, the concentrated solar hits a small area and the temperature in that area is the highest, and the further we move away from that area, the temperature will decrease more and more. There can be other factors that might influence the temperature of the system, such as the sun's position, the properties of the ambient air, the quality of the solar plant equipment and so on. However, despite all of those conditions, we can assume homogeneous temperatures on the hot and cold wall as we are only considering a fixed location, which covers only a small portion of the solar receiver (the yellow region in figure 3.1), thus we can assume that in the small area, the temperature of the walls does not vary temporarily [4].

The domain selected to perform the simulation is a three-dimensional domain (L_x*L_y*L_z) with following size:

$$L_x = 4\pi\delta;\ L_y = 2\delta;\ L_z = 4/3*\pi*\delta \text{ (where } \delta=3mm)$$

The temperature of the hot wall is T_h=1300K at y=2δ and the cold wall is T_c=900K at y=0. The cold wall temperature is quite high as well, since the extremely high temperature from the hot wall will radiate heat to the cold wall to increase its temperature as well, even though the cold wall is insulated from the ambient air. Thus, the channel flow will get heated from both the walls. The streamwise and the spanwise direction are periodic and the wall normal direction has non-uniform meshes. The reason for this condition is that the wall normal direction has a very strong thermal gradient condition due to the temperature difference between the hot and the cold wall. Thus, it is important to have a proper mesh configuration along the wall normal direction to investigate the case adequately. However, since the other two directions are periodic, there is an imbalance between the energy dissipation due to the viscous shear stress of the wall. The streamwise pressure gradient must be balanced for

this reason and a volume force in the streamwise direction is integrated in the flow to balance it with a streamwise friction. Thus, we can get a constant mass flow in the channel. Also, the thermodynamic pressure term P_0 is set to 10 bars with the mean wall friction Reynolds number being 800.

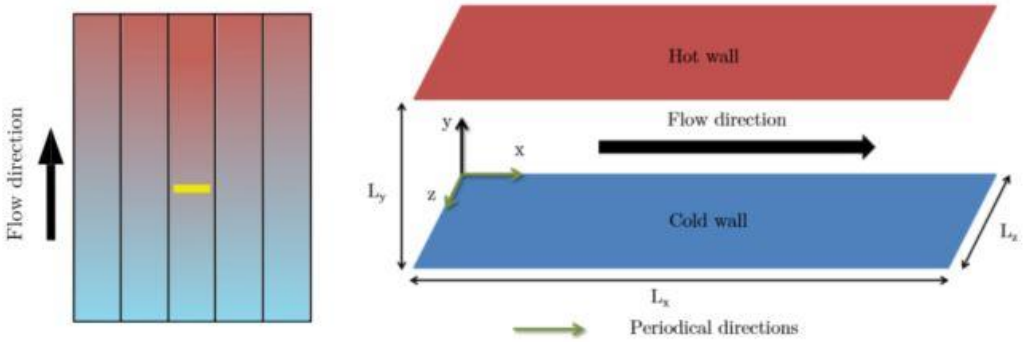

Figure 3.1: Anisothermal bi-periodic channel flow [4].

As previously mentioned, the wall normal direction has a strong temperature and velocity gradient and thus a non-uniform mesh is integrated in the wall normal direction to capture the information is a proper way. The other two directions (streamwise and spanwise) have uniform meshes. The mesh in the wall normal direction is calculated using the hyperbolic tangent relationship as stated below.

$$y_k = L_y\left(1+\frac{1}{a}tanh\left[\left(\frac{k-1}{N_y-1}-1\right)\tanh^{-1}(a)\right]\right), k \in [1, N_y] \quad (3.1)$$

Here, a is parameter called mesh dilatation, whereas N_y is the number of grid points along the wall normal direction of the channel configuration. Also, the heat flux condition considered for this study are given in Table.

Thermal Condition name	Heat sink (MW/m^3)	Hot wall heat flux (KW/m^2)	Cold wall heat flux (KW/m^2)
S0	0	98	-98

Table 3-1: Associated heat flux considered in this simulation.

In summary, the size of the domain for the channel flow is $4\pi\delta$ x 2δ x $4/3\delta$, where δ= 3mm. The temperature of the hold and cold wall are set to 1300K and 900k respectively. The thermodynamic pressure of the system is set to P_0=10 bars.

3.2. Multi scale approach

Out of different types of solar receiver, the receiver which uses pressurized air is still in a prototype stage, and the prospect of this type of solar receiver is promising. To properly commercialize this type of solar receiver, several optimizations are required to be done to integrate this into different functional renewable energy systems. Not only that, but solar receiver technologies also require very specialized tools to design and study the different scales of their functionality due to the complexity of these systems. To accelerate the commercialization of CSP plants using pressurized gas in the solar receivers, different scales of investigation are required. According to the literature description in [4], three stages of the investigation is crucial for the enhancement of the understanding of the correlation between the dynamic of the fluid flow and the temperature of the solar receiver to better optimize the system as a whole. The three levels, as depicted in **figure 3.2**, are the local level, the modular level, and the component level. Currently, the research focuses on maximizing heat transfer

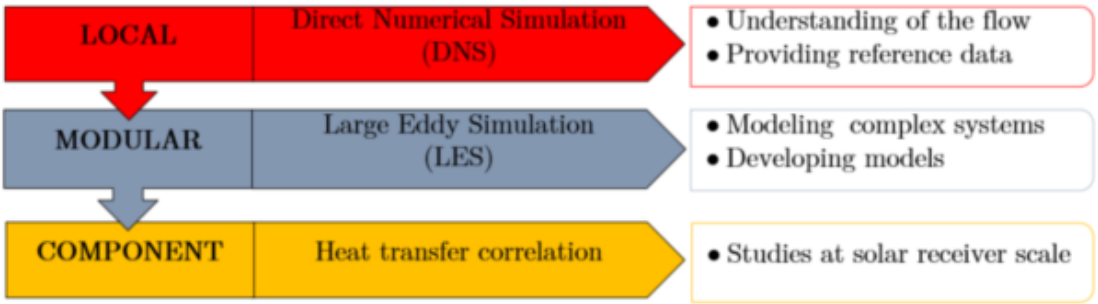

Figure 3.2: Problem Approach using multi-scale [4].

from concentrated sunlight to the flow of pressurized air in the solar receiver while also minimizing the pressure drops of the flow inside the channel. Out of the different levels of investigation, direct numerical simulation (DNS) provides extremely accurate results with fine level of details of all the turbulent scales of the process, but it also requires really high computational cost to do so [25][26][27]. However, another type of simulation called Large Eddy Simulation (LES) can be a much more cost effective and reliable option to access the heat transfer correlations of the gas pressurized solar receivers. In the LES method, the larger turbulent scales are computed, whereas the smaller scales that are most difficult to realize due to the requirements of finer meshes that are modeled using different LES models. These smaller scale models are called the sub-grid modeling. LES method simplifies the simulation to be able to simulate larger and more complicated geometries.

3.3. Simulation Approach

3.3.1. Navier Stokes Equations

For the purpose of simulating our problem, we needed to solve the Navier Stokes equations. Navier stokes equations are non-linear and partial differential equations which involves solving for the motion of the fluid that are viscous in nature. The Navier stokes equations consist of three equations of conservations. According to the mass conservation law, mass remains constant within an isolated system regardless of the chemical interactions or physical altercations. Mass cannot be created, nor it can be destroyed and the total amount of mass will always be unchanged as long as the system is an isolated system [28]. The second equation concerns the conservation of momentum, which implies that the sum of the momentum changes is balanced out by the sum of the external forces on the system [29]. Finally, the third equation related to energy conservation states that the variations of the total energy in the system are balanced by the external work and the exchange of the heat flux of the system with the surroundings [30].

- Mass conservation:

$$\frac{\partial \rho}{\partial t} + \frac{\partial \rho U_j}{\partial x_j} = 0 \qquad (3.2)$$

- Momentum conservation:

$$\frac{\partial \rho U_j}{\partial t} = -\frac{\left(\partial \rho U_i U_j\right)}{\partial x_j} + \frac{\partial \Upsilon_{ij}}{\partial x_j} \qquad (3.3)$$

- Energy conservation:

$$\frac{\partial \rho (E+I)}{\partial t} = \frac{\partial \rho U_j (E+I)}{\partial x_j} - \frac{\partial Q_j}{\partial x_j} + \frac{\partial \Upsilon_{ij} U_i}{\partial x_j} \qquad (3.4)$$

Here, i index is used to symbolize the i-th direction, x is the cartesian coordinate, Υ_{ij} is the total stress tensor component, Q is the conductive heat flux, t is the time, I indicate the internal energy per mass-unit, and E is the kinetic energy per mass-unit.

The term Υ_{ij} is composed of pressure component and viscous component, thus it can be written as:

$$\Upsilon_{ij} = -P\delta_{ij} + \Sigma_{ij} \qquad (3.5)$$

As for Newtonian fluid, the local strain and the viscous stresses are linearly correlated. Using the Stokes law [4], we can write this relationship like the following,

$$\Sigma_{ij} = 2\mu S_{ij} - \frac{2}{3}\mu S_{kk}\delta_{ij} \qquad (3.6)$$

Where, μ is the dynamic viscosity and S_{ij} is the deformation tensor, whose expression can be written as the following,

$$S_{ij} = \frac{1}{2}\left(\frac{\partial U_i}{\partial x_j} + \frac{\partial U_j}{\partial x_i}\right) \qquad (3.7)$$

In terms of the heat flux due to conduction, according to the Fourier's law [31], we can write,

$$Q_j = -\lambda \frac{\partial T}{\partial x_j} \qquad (3.8)$$

Where, T is the temperature and λ denotes the thermal conductivity.

There are alternate formulations of the energy conservation equation and the temperature transport equation can be written as the following [32],

$$C_v \frac{\partial \rho U_j}{\partial t} = -C_v \frac{\partial \rho U_j T}{\partial x_j} - \frac{\partial Q_j}{\partial x_j} - \beta P T \frac{\partial U_j}{\partial x_j} + \Sigma_{ij} \frac{\partial U_i}{\partial x_j} \qquad (3.9)$$

Where C_v is the heat capacity at constant volume. Since the whole system consists of eight (ρ, U, V, W, T, P, λ, μ) variables and the Navier-Stokes itself has fives equations, three more equations are needed to close the system and solve it.

One of the three equations for this particular study is the idea gas law, which is the accumulation of different laws such as Boyle's law, Charles's law etc. [33]. The idea law under a series of hypotheses can be related temperature, pressure, and density of a certain ideal gas. Since in our case, we are using pressurized air, we can use the ideal gas law for closing the system of equations. The ideal gas law is stated as follows,

$$P = \rho r T \qquad (3.10)$$

Here, r is the specific gas constant for pressurized air. In terms of an ideal gas, the heat capacities can be related to the specific gas constant such as, $C_p - C_v = r$. This relationship only depends on the temperature. Also, the constant pressure and constant temperature thermal expansion coefficient are equal and can be respectively written as, α=β=1/T [4].

One more equation can be considered using the Sutherland's law that permits us to calculate the dynamic viscosity of the pressurized air using a correlation of temperature [34]. The equation is state as follows,

$$\mu(T) = \mu_0 \frac{T^{3/2}}{T_0} \frac{T_0 + S}{T + S} \qquad (3.11)$$

The values of the constants in the equation are, T_0=273.15K, S=110.4K and μ_0=1.716x10^{-5} Pa.s.

Finally, to close the equations, we need an equation to calculate the value of the thermal

conductivity. We can do that using the Prandtl number, isobaric heat capacity value and the value of the viscosity which we get from the previous equation [4],

$$\lambda(T) = \frac{C_p}{Pr}\mu(T) \qquad (3.12)$$

3.3.2. Low Mach Assumption

The Navier stokes equation becomes much simpler if the flow is incompressible, which gives a different equation with less complications compared to the compressible flow equation. For the compressible flow, the density is not constant over time. Since our problem is related to a solar receiver with pressurized air, the density changes over time due to the high fluctuation of temperature along the receiver. However, to simplify the equation of the compressible flows further, Paolucci [35] in 1982 proposed an assumption that utilized the low Mach number assumption to reduce the difference between the equations of the incompressible and compressible fluid flow Navier-Stokes equation. Usually in the Boussinesq's formula, the compression forces are neglected and only the hydrostatic buoyancy is considered in the equations. However, this method has a limitation regarding the temperature of the application, as this method is only suitable for problems that has relatively less temperature fluctuation (ΔT<30K) [36], [37]. For solar receiver applications, the variation of temperature is not within this range by a large margin. The low Mach number assumption is suitable for this reason, as this method considers the application of large density gradient problems into the equation. The low Mach number assumption tries to neglect the acoustic waves propagation inside the flow while describing the internal wave propagation of the flow. Neglecting the acoustic waves from the equation simplifies it and removes many constraints that might have occurred if compressible flow equations were used instead. Thus, after removing the constraints, the incompressible flow equations can be used.

The Mach number is the ratio between the speed of the flow and the speed of the sound for a particular temperature and medium, and it can be written as,

$$Ma = \frac{U_*}{c_*} \qquad (3.13)$$

For ideal gases, equation for the speed of sound for a specific temperature and medium can be written as, $c_* = \sqrt{\gamma r T_*}$. Depending on the value of the Mach number, a flow speed can be identified as subsonic, sonic, or supersonic flow. The concept behind Paolucci's [35] low Mach number assumption is to consider any flow with Mach number below 0.3 as a low Mach number flow. Later, the N-S equations are non-dimensionalized and all the dimensionless numbers are later expanded through a power series of the squared Mach number. Later, the higher order Mach number terms are truncated and are not considered anymore.

3.3.2.1. Non-Dimensionalized Navier-Stokes Equations

To non-dimensionalize each term, a characteristic value of each term has to be selected. Assuming X being a variable, X^0 being the non-dimensional variable and X* being the characteristic value of the variable, we can write,

$$X^0 = \frac{X}{X_*} \qquad (3.14)$$

For the equations we are considering, the variable X can be successively t, U, L, P, T, C_v, C_p, ρ, μ and λ.

Using three numbers that are dimensionless and characterize the flow, we can define Reynolds number that signifies the ratio between convective forces and viscous forces in a fluid flow.

Another dimensionless number called Prandtl number is used, which signifies how much the convective diffusivity has influence on a flow compared to the thermal diffusivity. It can be written as,

$$Pr = \frac{\mu_* C_{p_*}}{\lambda_*} \qquad (3.15)$$

Using the method of non-dimensionalization, the Navier stokes equations can be written as:

- Mass conservation

$$\frac{\partial \rho^0}{\partial t^0} + \frac{\partial \rho^0 U_j^0}{\partial {x_j}^0} = 0 \qquad (3.16)$$

- Momentum conservation

$$\frac{\partial \rho^0 U_i^0}{\partial t^0} = -\frac{\partial \rho^0 U_j^0 U_i^0}{\partial {x_j}^0} - \frac{1}{\gamma Ma^2}\frac{\partial P^0}{\partial {x_i}^0} + \frac{1}{Re}\frac{\partial {\Sigma^0}_{ij}}{\partial x_j} \qquad (3.17)$$

- Energy conservation

$$C_v^0 \frac{\partial \rho^0 T^0}{\partial t^0} = -C_v^0 \frac{\partial \rho^0 U_j^0 T^0}{\partial {x_j}^0} - \frac{\gamma}{Pe}\frac{\partial Q_j^0}{\partial {x_j}^0} - (\gamma - 1)P^0 \frac{\partial U_j^0}{\partial {x_j}^0} + \gamma(\gamma - 1)\frac{Ma^2}{Re}{\Sigma^0}_{ij}\frac{\partial U_i^0}{\partial x_j} \qquad (3.18)$$

Where, Pe is called the Peclet number and it is written as $Pe = RePr$, which signifies the ratio between the convection heat transfer and the conductive heat transfer.

- Ideal gas law

$$P^0 = \rho^0 T^0 \qquad (3.19)$$

$$\Sigma^0{}_{ij} = 2\mu^0 S^0{}_{ij} - \frac{2}{3}\mu^0 S^0{}_{kk}\delta_{ij} \qquad (3.20)$$

$$Q^0{}_j = -\lambda^0 \frac{\partial T^0}{\partial x_j{}^0} \qquad (3.21)$$

Here, the term $\Sigma^0{}_{ij}$signifies the viscous stress tensor and $Q^0{}_j$ as the conductive heat flux as non-dimensional terms.

3.3.2.2. Dimensioned low-Mach number Navier-Stokes Equations

As according to Paolucci [38], in a power series, all the different variables can be expressed as the power series of the square of Mach number. For the purpose of the study, the Mach number is categorized as a low Mach number value, thus the terms that are on higher order than the squared of the Mach number are truncated and neglected. Thus, equations (**3.16)-(3.19)** can be re-dimensionalized to get the equations for low Mach number:

- Mass conservation

$$\frac{\partial \rho}{\partial t} + \frac{\partial \rho U_j}{\partial x_j} = 0 \qquad (3.22)$$

- Momentum conservation

$$\frac{\partial \rho U_i}{\partial t} = -\frac{\left(\partial \rho U_i U_j\right)}{\partial x_j} - \frac{\partial P}{\partial x_i} + \frac{\partial \Sigma_{ij}}{\partial x_j} \qquad (3.23)$$

- Energy conservation

$$\frac{\partial U_j}{\partial x_j} = -\frac{1}{\gamma P_0}\left[(\gamma - 1)\frac{\partial Q_j}{\partial x_j} + \frac{\partial P_0}{\partial t}\right] \qquad (3.24)$$

- Ideal gas law

$$T = \frac{P_0}{\rho r} \qquad (3.25)$$

The pressure P_0 is the mean pressure of the domain of the computation, which is also denoted as the thermodynamic pressure of the system. The thermodynamic pressure depends on the time and not on the spatial coordinates of the system $(\frac{\partial P_0}{\partial x_i} = 0)$[4]. This term is defined using the gas law for ideal cases, whereas another pressure term P, which appears in equations like the momentum conservation equation is called the Mechanical pressure, which varies along the spatial coordinates. The thermodynamic pressure P_0, however, is constant.

3.3.2.3. Heat Source

Concentrated solar plant towers usually utilize the radiation of the solar energy by concentrating all the solar irradiation on the front of the solar receiver of the solar tower. The solar receiver absorbs most of the energy from the concentrated solar irradiation, and

this solar energy is converted to heat energy instead. The temperature of the solar receiver usually goes up to a high number, and this heat is transferred to the fluid passing through the solar receiver by the heat transfer mode called conduction. Although the solar irradiation is all concentrated on the front wall of the solar receiver and the opposed wall is totally insulated from the atmosphere and the atmospheric air, the extreme high temperature of the front wall induces significant amount of radiative heat transfer, which increases the temperature of the opposed wall as well. Thus, instead of the fluid being heated by only the front wall, the fluid is usually heated by both sides of the wall in real cases. This is an important factor that needs to be considered while considering the simulations.

For this study, out of the three directions, only the wall normal direction is not considered periodical, and the other two directions have periodical conditions. Thus, the channel flow is a bi-periodical channel flow problem, and this lets us simulate different locations of the solar receiver at various sections. However, this condition implies that the flow is a fully developed flow and to compensate for the impact of the walls and thermal development inside the flow, we need to add an extra heat source term. The heat source terms gives us a flexibility of studying different thermal profiles and different axial positions inside the solar receiver, which is beneficial for comprehensive studies of the system [4]. If we add the source term H_s into the energy conservation equation of the N-S, we get the following equation.

$$\frac{\partial U_j}{\partial x_j} = -\frac{1}{\gamma P_0}\left[(\gamma - 1)\left(\frac{\partial Q_j}{\partial x_j} - H_s\right) + \frac{\partial P_0}{\partial t}\right] \qquad (3.26)$$

3.4. Numerical Setup

The resolution of the Navier stokes equation when the flow is not incompressible and laminar is still an unknown field. The Navier stokes equations are one of the problems are called Millenium prize problems, which means that the search for the general solution of this equation is still non-existent [39]. However, for simple geometries and laminar flows, analytical solutions can be found. For incompressible flows, there are procedures of getting weak solutions, which was demonstrated by Leray et al[40].

For this study, the investigation is related to turbulent flows where the kinetic energy of the flow is more dominant compared to the viscosity of the flow. Thus, the kinetic force of the flow can overcome the viscous forces. Thus, these kinds of flows do not have any analytical solution using Navier Stokes equations. To characterize these kinds of flows, we still must depend on experimentation and numerical simulations. Turbulent flows have irregular and unpredictable behaviors with different scales of time and space [41]. Also, the fluid flow described by the Navier stokes equations are continuous in nature, whereas the numerical solutions can solve equations which are discrete systems. For that particular reason, the equations as well as the computational domains need to be discretized.

Resolved Algorithm of solving the discretized equations is described below:

1. Using the mass conservation relationship from the Navier stokes, the density term is calculated,

$$\rho^{n+1} = -\Delta t[\nabla.(\rho^n U^n)] + \rho^n \qquad (3.27)$$

2. To determine the thermodynamic pressure and then the value of temperature using ideal gas law, fixed point iteration is used. A value of k between 0 and 3 is used for this purpose. The value if k is an empirical value assumption which has been determined in order to obtain convergence for this kind of simulations [4]. To calculate the thermodynamic pressure, the energy equation is used by integrating this equation around the entire domain with the heat source term included in the equation.

$$\frac{1}{\gamma - 1}\frac{dP_0}{dt} = \frac{1}{V}\int_V \frac{\partial Q_j}{\partial x_j} - H_s dV \qquad (3.28)$$

Later, the divergence theorem is used to convert the volume integral into a surface integral and thus the equation is discretized, to:

$$P_0^{n+1,k+1} = \frac{P_0^n}{1 - (\gamma - 1)\frac{\Delta t}{P_0^{n+1,k}}\left(\frac{1}{V}\int_\omega \lambda_\omega \nabla T^{n+1,k} dS - H_s\right)} \qquad (3.29)$$

3. After calculating the density and the thermodynamic pressure, we can now use these two values in the ideal gas law to calculate the temperature,

$$T^{n+1,k+1} = \frac{P_0^{n+1,k+1}}{r\rho^{n+1}} \qquad (3.30)$$

4. Using the Sutherland's law, we can calculation the dynamic viscosity with the temperature which we calculated in the previous step,

$$\mu^{n+1} = \mu^0 \left(\frac{T^{n+1}}{T_0}\right)^{\frac{3}{2}} \frac{T_0 + S_1}{T^{n+1} + S_1} \qquad (3.31)$$

5. Using the dynamic viscosity and Prandtl number, we can now calculate the thermal conductivity,

$$\lambda^{n+1} = \frac{\mu^{n+1} C_p}{Pr} \qquad (3.32)$$

6. Later, the velocity divergence term can be calculated using the energy conservation law from the Navier stokes equation,

$$\nabla.U^{n+1} = \frac{1}{\gamma P_0^{n+1}}\left[(\gamma - 1)(\nabla.(\lambda^{n+1}\nabla T^{n+1}) - H_s) - \frac{P_0^{n+1} - P_0^n}{\Delta t}\right] \qquad (3.33)$$

7. Using the projection method steps, we can now calculate the intermediate velocity using the momentum conservation without the mechanical pressure term in the equation,

$$U^* = \frac{\Delta t}{\rho^n}\left[U^n\nabla.(\rho^n U^n) - \nabla.(\rho^n U^n U^n) + \nabla.\left(\mu^n(\nabla U^n + \nabla^T U^n)\right) - \frac{2}{3}\nabla(\mu^n \nabla. U^n)\right] + U^n \qquad (3.34)$$

8. Using the divergence of the intermediate velocity we just calculated in the previous step, the mechanical pressure term can be calculated,

$$\nabla.\left(\frac{1}{\rho^n}\nabla P^{n+1}\right) = \frac{\nabla. U^* - \nabla. U^{n+1}}{\Delta t} \qquad (3.35)$$

9. Finally, in the last step, the velocity value is corrected using the mechanical pressure in the momentum conservation relations.

$$U^{n+1} = -\frac{\Delta t}{\rho^n}\nabla P^{n+1} + U^* \qquad (3.36)$$

For performing simulations, the continuous Navier-Stokes equations had to be discretized using numerical schemes for time derivatives and spatial derivatives. There are large quantities of studies that present the significance of the schemes for discretization of the equations for LES [42][43][44][45] and DNS [46][47] simulations. For the mass conservation equation of the Navier Stokes, the second order discretization scheme was used, whereas for the momentum equation, second and fourth order discretization scheme can be chosen.

Temporal stability criteria, especially for explicit time integration methods are crucial so that the numerical analysis converges properly without issues. The timestep of each iteration has to be calculated after each iteration to maintain the criteria of stability. The stability criterion is mainly considered by focusing on the stability requirements for the conservation of momentum equations since the energy equation of the Navier stokes equation puts constraints on the pressure as we can see in the resolution algorithm [4]. For the temporal stability, the CFL condition or the Courant-Friedrichs-Lewy condition is a crucial condition for numerically solving different kinds of partial differential equations [48]. Thus, the purpose of the condition is to keep the time step below a certain range on purpose so that all the information necessary to resume the solution in the next steps may have time to propagate in the space discretization as well. This way all the necessary physical information will be present in the next timesteps which will eventually affect the trend of the solution from the previous steps. The stability equation for convection is given below,

$$\frac{1}{\Delta t_{conv}} = max_{x,y,z}\left[\frac{U_x}{\Delta x} + \frac{U_y}{\Delta y} + \frac{U_z}{\Delta z}\right] \qquad (3.37)$$

Similarly, the stability equation for diffusion is given below,

$$\frac{1}{\Delta t_{diff}} = max_{x,y,z}\left[2\nu\left(\frac{1}{\Delta x^2} + \frac{1}{\Delta y^2} + \frac{1}{\Delta z^2}\right)\right] \qquad (3.38)$$

To meet the stability criterion for both diffusion and convection, the final time step of the numerical simulation has to be half of the harmonic mean between the stability timestep of both convection and diffusion [4],

$$\frac{1}{\Delta t} = \frac{1}{\Delta t_{conv}} + \frac{1}{\Delta t_{diff}} \qquad (3.39)$$

For the next steps of the iterations, the time step is updated further for two conditions:

a) If the next time step is smaller than the previous time step value.
b) If the current and previous timestep values have a relative difference of more than 5%.

3.5. Processing of Data

Turbulent flows are inherently highly unorganized, unpredictable, and chaotic. Even with close initial boundary conditions, different experimentation and simulations end up giving different results. To properly analyze the data generated due to the experimentation and simulation of turbulent flow characteristics, and method called Reynold's decomposition is generally used. For an instantaneous variable f, it can be decomposed down to two parts, a mean part <f> and the rest is the fluctuation f'. Thus, any instantaneous variable f can be written as,

$$f = \langle f \rangle + f' \qquad (3.40)$$

It is assumed that performing a statistical mean on the fluctuating part of the decomposition will lead to zero. We can perform Reynolds averaging to the simulation result of an instantaneous variable to get the mean value of the variable. This method lets us separate the fluctuations from the mean and following the ergodicity hypothesis proposed by Boltzmann (1871). This hypothesis offers a way to calculate the Reynolds average with an average across the time when the flow is fully developed [4].

$$\langle f \rangle = \lim_{N \to \infty} \frac{1}{N} \sum_{i=1}^{N} f_i \qquad (3.41)$$

3.6. Validation Process

As of our knowledge, for this condition of a solar receiver with pressurized air in the channel flow, there is no reference data in terms of experimentations to compare with the LES simulations results. Thus, for this thesis, the results of the performed LES methods are going to be compared with the exiting DNS results for the same conditions.

4. LES Approach

4.1. Principles of LES

The main principle of the large eddy simulation is that the LES method mainly considers the large-scale eddies and only resolves these scales in the simulation. The smaller scales are not resolved in the LES algorithm and they are later compensated by only considering the effect of the smaller scales of eddies on the larger eddies [49][50][51]. The smaller scales are filtered out using a spatiotemporal filter to resolve the larger scales [52]. The smaller scales are later modeled using different LES models to get better results. The LES that integrates with algebraic models uses the universality of smaller scales assumption, which states that the smaller scales are totally independent from the effect of the larger scale eddies on them [53]. Another important assumption is that the smaller scale structures possess very little kinetic energy on their own, they are unaffected by both the thermal conditions of the domain that LES is studying and the large structure mechanisms. Thus, from these characteristics, it can be assumed that the small scales are very much self-similar and are isotropic in behaviors [54].

For LES methods, the error can be decomposed into three most important errors, which are accumulated when the Navier stokes equations are discretized [50]. The errors generated while solving the N-S equations can be calculated by summing these three types of errors. These three errors are projection error, discretization error and resolution error. The projection error, err_π occurs due to having finite degree of freedoms while the solution is obtained. The second error, which is the discretization error err_d, occurs when the continuous partial differential equations are approximated and discretized to solve them in discrete domains for computational convenience. Finally, the resolution error occurs to performing LES, which filters out the smaller scales from the exact solution, hence the resolution of the solution is not accurate enough and is not exact. This error is called the resolution error err_r. Thus, the total error, err can be summarized as,

$$err = err_\pi + err_d + err_r \qquad (4.1)$$

Out of all these errors, the projection error will always be present, and we cannot avoid it. To reduce the error of the LES method, the other two errors, which means the discretization error and the resolution error must be omitted or reduced. This can be performed by using one of two ways.

- There is an LES method called Implicit LES (ILES), which tries to cancel out discretization error and resolution error by each other by finding a balance between them. Thus, it can be written as,

  $$err_d + err_r = 0 \qquad (4.2)$$

  When using the ILES, the resolved equations do not introduce further sub grid

models. The truncation error that occurs due to the truncation of the higher order terms of the numerical schemes acts as its own compensation for the sub-grid scales. This numerical model called ILES is usually chosen for balancing out the discretization error and the resolution error [55].

- However, classically when LES method is mentioned, this second approach called Explicit LES is used more compared to the ILES. In this method, both the resolution error and the discretization error are focused to be individually canceled out, rather than using both errors to cancel each other out like the previous method. Thus, it can be written as,

$$err_d = err_r = 0 \qquad (4.3)$$

The errors caused by the discretization are reduced or omitted using numerical methods, but the resolution error is compensated by different LES models by an additional term, which is introduced in the Navier Stokes equation. This additional term or model tries to account for the effects of the smaller scales, in other words the high frequency modes which were filtered out due to the spatiotemporal filter as the filter only resolves the larger scale structures or the low frequency modes.

There are two different kinds of LES models. One of them is called functional models, which tries to focus on the transfer due to kinetic energy. The other one is called structural models, which tries to calculate the structure of the tensor at sub grid scale [50]. More details and different kinds of analyses are presented in [56][57][58][59] if the reader is interested further.

4.2. Turbulence Filtering

4.2.1. Filter Properties

As previously mentioned, the LES method uses a spatiotemporal filter to filter out the smaller scales and only tries to resolve the larger scales of the eddies. The smaller scales are later modeled for considering the impact of the smaller eddies on the larger eddies. This scale separation using a low pass frequency filter reduces the computation load by a lot, as highly turbulent flows include too many structures at the smaller scales. A convolution product is included with the filter of LES method. For the purpose of simplifying the system, it is considered that the filter is isotropic, that is the properties are given for a case that is homogeneous. For any particular field, the filtered field $\bar{\psi}$ can be defined as,

$$\bar{\psi}(x,t) = \int_{-inf}^{inf} \int_{-inf}^{inf} \psi(\xi,\tau) G(x-\xi, t-\tau, x, t) d\xi d\tau \qquad (4.4)$$

Where, G indicates the convolution kernel. For the resolved part, the expression can be written as,

$$\bar{\psi} = G * \psi \qquad (4.5)$$

Similarly, if the resolved part is written as $\bar{\psi}$, the main field is denoted as ψ, then the unresolved part ψ' can be calculated as,

$$\psi'(x,t) = \psi(x,t) - \bar{\psi}(x,t) \qquad (4.6)$$

$$\psi'(x,t) = \psi(x,t) - G * \psi(x,t) \qquad (4.7)$$

In most of the simulations involving LES, time and spatial filtering is not applied separately, rather only spatial filtering is applied during the process of LES. This is done as spatial filtering automatically induces time filtering in an implicit manner [60][61].

This kind of filters has to maintain three properties:

1. Constant Conservation property
$$\bar{C} = C \qquad (4.8)$$
2. Property of Linearity, which satisfies the convolution products by definition. For any fields ψ_1 and ψ_2,
$$\overline{\psi_1 + \psi_2} = \overline{\psi_1} + \overline{\psi_2} \qquad (4.8)$$
3. Property of commutation for spatial derivatives and temporal derivatives:
$$\frac{\overline{\partial\psi}}{\partial x} = \frac{\partial\bar{\psi}}{\partial x} \qquad (4.9)$$
$$\frac{\overline{\partial\psi}}{\partial t} = \frac{\partial\bar{\psi}}{\partial t} \qquad (4.10)$$

However, the commutation property for the temporal derivative is respected in all cases, but the same does not occur for spatial derivatives, unless the filter is isotropic [62]. For LES method, filters such as Sharp spectral filter, box filter, gaussian filter etc. are used [63].

4.2.2. Implicit and Explicit filtering

There are two types of filtering that can be associated with the LES method, one is explicit filtering and the other is implicit filtering. In terms of the explicit filtering, the convective term is targeted by the explicit filter, and it lowers the number of scales during the solution. While doing so, the explicit filtering method can restore a spectral content which is consistent to each term of the filtered N-S numerical solution. This method reduces the effect of the filtering on the numerical error of the solution, along with the grid characteristics as the method has a filter length which is explicit. The length of the filter must be taken in such a way that it should be bigger than the local sizes of cells. This filtering method reduces the resolve scale spectrum and dampens the motion of the small scales which were admitted by the meshes [23][64][65][66][27].

For implicit filtering process, this filter is obtained from the meshes, sub-grid scale models, resolved equations and numerical method in an implicit manner, while having no well-defined shape of the filter. There are advantages and disadvantages of using the implicit filtering method. One of the key disadvantages is that the numerical error cannot be

controlled, and filtering can be performed along a single direction, and that is the direction of the compound derivative. For this reason, another supplementary filter is needed with one-dimensional characteristics to all the terms in the equation of LES. Furthermore, the actual equation which is going to be solved cannot be derived from the N-S equations in a rigorous manner. Despite all the disadvantages, implicit method is mostly used and more classical way of using a filter. Implicit method reduces the computational cost significantly when compared to explicit filtering, by taking the benefit of the grid resolution and avoiding the calculation of the model term at sub grid scale [67][68][69][70][56].

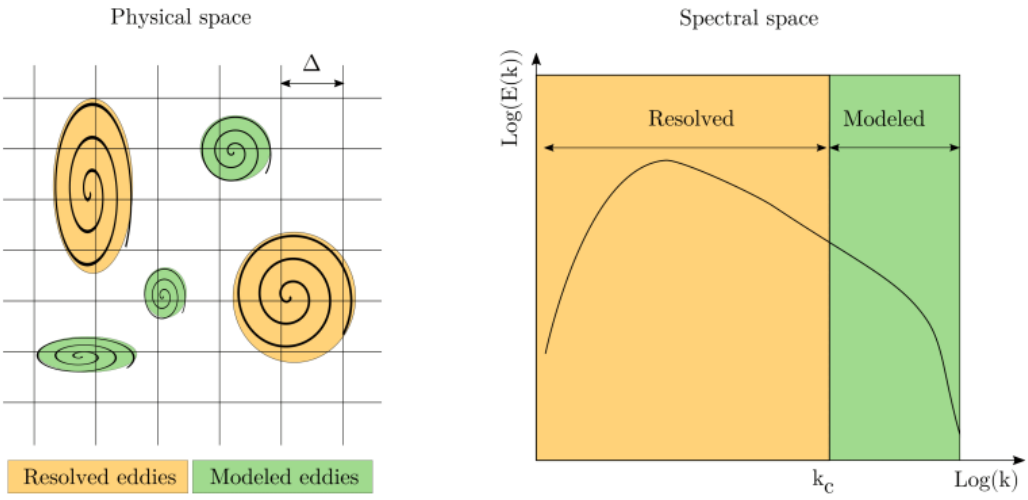

Figure 4.1: Separation of scales along spectral and physical space [50].

4.2.3. Resolved Equations

As previously mentioned, for this study time filtering is not separately used, rather an implicit spatial filtering is used, which induces time filtering as well. On the computational grid, the length of the filter is derived by discretizing the N-S equations and it can be written as,

$$filter\ length, \Delta = \sqrt[3]{\Delta_x \Delta_y \Delta_z} \qquad (4.11)$$

Where, $\Delta_x, \Delta_y, \Delta_z$ are the sizes of the mesh along x, y and z coordinates respectively. The filters that are involved in the mesh sizes along with the filter which is induced by errors of the numerical calculation and modelling stems the application of filtering on the exact solution. As we can see in **figure 4.1**, the filtering has been applied in the LES method. The figure has described the filtering using two different perspectives. In the first one, a physical space is being imagined where the eddies that are smaller than 2Δ are modeled, and the rest of the bigger scales are resolved. On the other hand, in the right side of **figure 4.1**, the filtering is represented by spectral space, where the wavenumber has a cutoff frequency, $k_c = \pi/\Delta$. The scales having smaller wavenumber than the cutoff frequency is resolved and the scales with bigger wavenumber compared to the cutoff value are modeled. The

right figure shows a plot between the kinetic energy E as the dependent variable and the wavenumber of the scales, k as the independent variable on the horizontal axis. As we can see in **figure 4.1**, the scales on the right side of k_c are all modeled, which signifies the smaller scale eddies.

Now, if we take the low Mach number equations and apply the filter, we get,

1. Conservation of mass

$$\frac{\partial \bar{\rho}}{\partial t} + \frac{\overline{\partial \rho U_J}}{\partial x_j} = 0 \qquad (4.12)$$

2. Conservation of momentum

$$\frac{\partial \overline{\rho U_J}}{\partial t} = -\frac{\overline{\partial \rho U_J U_\iota}}{\partial x_j} - \frac{\overline{\partial P}}{\partial x_i} + \overline{\frac{\partial}{\partial x_J}\left[\mu\left(\frac{\partial U_\iota}{\partial x_J} + \frac{\partial U_J}{\partial x_J}\right)\right]} - \frac{2}{3}\overline{\frac{\partial}{\partial x_\iota}\mu\left(\frac{\partial U_J}{\partial x_J}\right)} \qquad (4.13)$$

3. Conservation of energy

$$\frac{\overline{\partial U_J}}{\partial x_J} = -\frac{1}{\gamma P_0}\left[(\gamma - 1)\,\overline{\frac{\partial}{\partial x_J}\left(-\lambda\frac{\partial T}{\partial x_J}\right)} + \frac{dP_0}{dt}\right] \qquad (4.14)$$

4. Law of ideal gas

$$P_0 = r\overline{\rho T} \qquad (4.15)$$

We know that the thermodynamic pressure P_0 is constant spatially, thus a spatial filter would not change anything for this term, and we will get, $\overline{P_0} = P_0$.

4.2.4. Favre Average

In terms of the solar receiver, we intend to study in this thesis, the working fluid is pressurized gas. For this case, the density and the temperature of the working fluid is varying at a large extent. Thus, a filter called Favre average is used for suitability, which is a density based filter [71]. The concept behind the Favre average is, this uses an incompressible decomposition, and extends it to the case which is compressible by introducing an average density-weighted system [72][73]. If the Favre average is applied on a variable called X, it can be written as,

$$\tilde{X} = \frac{\overline{\rho X}}{\bar{\rho}} \qquad (4.16)$$

Where, the $\widetilde{(.)}$ sign is used to denote that the Favre average has been applied.

As we have previously seen, the filters must follow the commutation rules. If we assume that the filters follow the commutation rules, the low Mach number equations with the Favre filtering will give us the following equations,

1. Conservation of mass

$$\frac{\partial \bar{\rho}}{\partial t} + \frac{\overline{\partial \rho} \widetilde{U_J}}{\partial x_j} = 0 \qquad (4.17)$$

2. Conservation of momentum

$$\frac{\partial \bar{\rho} \widetilde{U_\iota}}{\partial t} = -\frac{\partial \bar{\rho} \widetilde{U_J U_\iota}}{\partial x_j} - \frac{\partial \bar{P}}{\partial x_i} + \frac{\partial}{\partial x_j}\left[\bar{\mu}\left(\frac{\partial \widetilde{U_\iota}}{\partial x_j} + \frac{\partial \widetilde{U_J}}{\partial x_j}\right)\right] - \frac{2}{3}\frac{\partial}{\partial x_i}\left(\bar{\mu}\frac{\partial \widetilde{U_J}}{\partial x_j}\right) \qquad (4.18)$$

3. Conservation of energy

$$\frac{\partial \widetilde{U_J/\rho}}{\partial x_j} = -\frac{1}{\gamma P_0}\left[(\gamma - 1)\frac{\partial}{\partial x_j}\left(-\lambda(\tilde{T})\frac{\partial \tilde{T}}{\partial x_j}\right) + \frac{dP_0}{dt}\right] \qquad (4.19)$$

4. Law of ideal gas

$$P_0 = r\bar{\rho}\tilde{T} \qquad (4.20)$$

As we can see, there are two terms that are still unresolved: $\widetilde{U_J U_\iota}$ and $\widetilde{U_J/\rho}$.

Applying Leonard decomposition [74] on the above momentum equation we get,

$$\frac{\partial \bar{\rho} \widetilde{U_\iota}}{\partial t} = -\frac{\partial \bar{\rho} \widetilde{U_J} \widetilde{U_\iota}}{\partial x_j} - \frac{\partial \bar{P}}{\partial x_i} + \frac{\partial}{\partial x_j}\left[\bar{\mu}\left(\frac{\partial \widetilde{U_\iota}}{\partial x_j} + \frac{\partial \widetilde{U_J}}{\partial x_j}\right)\right] - \frac{2}{3}\frac{\partial}{\partial x_i}\left(\bar{\mu}\frac{\partial \widetilde{U_J}}{\partial x_j}\right) - \frac{\partial \bar{\rho} G_{U_j U_i}}{\partial x_j} \qquad (4.21)$$

Where,

$$G_{U_j U_i} = \widetilde{U_J U_\iota} - \widetilde{U_J}\widetilde{U_\iota} \qquad (4.22)$$

Similarly, Applying the Leonard decomposition in the energy equation we get,

$$\frac{\partial \widetilde{U_J}}{\partial x_j} = -\frac{1}{\gamma P_0}\left[(\gamma - 1)\frac{\partial}{\partial x_j}\left(-\lambda(\tilde{\rho})\frac{\partial \tilde{T}}{\partial x_j}\right) + \frac{dP_0}{dt}\right] - \frac{\partial \bar{\rho} G_{\frac{U_j}{\rho}}}{\partial x_j} \qquad (4.23)$$

Where,

$$G_{U_j/\rho} = \widetilde{U_J/\bar{\rho}} - \frac{\widetilde{U_J}}{\bar{\rho}} \qquad (4.23)$$

These two equations are not closed; hence we need to express these terms as the features of the fields that are filtered and resolved. The term $G_{U_j U_i}$ is the velocity-velocity correlation and $G_{U_j/\rho}$ is the velocity-density correlation. These two terms account for the sub grid terms that have not been resolved.

4.3. Sub-grid Scale (SGS) models

In the case of the LES method, the main equations are solved for the characteristics of the large scales after using the filter on the N-S equations. The commutations of the filtering and the differentiation must follow structures similar to the N-S equations. However, as we previously mentioned, the commutation rule for the derivatives is not maintained when the width of the filter is not uniform [75][76]. This phenomenon occurs when turbulent flows are not homogeneous, thus the smallest size of the eddies depends on the location of the region that needs to be studied. Since the smallest scale varies spatially, thus the filter width is also dependent spatially. Thus, the introduction of nonuniform filter requires supplementary sub-grid terms to balance the commutation of the system. The sub-grid terms are not linear and have to be modeled as direct calculation of these terms is not possible.

The main principle is that the LES method should maintain the necessary characteristics of the N-S equations. The N-S equations go through different kinds of transformations along the coordinates, however the fluid characteristics do not change regardless of the transformation along the coordinates, which means that N-S equations are reference frame independent while maintaining the conservation laws and the proper scaling [77]. The LES method along with sub-grid scale models has to maintain these characteristics as well [78][79].

After applying Favre's average to the low Mach number equations, we manage to derive two major sub-grid terms from the momentum and energy conservation equations. These two sub-grid terms are $G_{U_jU_i}$ which is the velocity-velocity correlation and $G_{U_j/\rho}$ which is the velocity-density correlation. The eddy-viscosity concept that depends on different flow characteristics functions as the fluid motion itself dictates the behavior of turbulence. The eddy-viscosity concept can be algebraically realized using zero equation, or one or multiple transport equations, which can be denoted as n-equation models for turbulence, where n signifies the number of equations that are being used to realize the eddy-viscosity model [79][80][81][82]. For this study, zero-equation models are used. The velocity-velocity and the velocity density correlations respectively can be represented as:

$$G_{U_jU_i} = \tau_{ij}^{mod}\left(\tilde{U}, \bar{\Delta}\right) \qquad (4.24)$$

$$G_{U_j/\rho} = \pi_j^{mod}\left(\tilde{U}, \frac{1}{\bar{\rho}}, \bar{\Delta}\right) \qquad (4.25)$$

4.3.1. Functional Models

The main principle of the functional models is that it tries to approximate the forward energy cascade phenomenon by introducing a diffusive term [83] and tries to reproduce the effect sub grid scale eddies have on the larger resolved scales. Apart from that, an additional

diffusion is introduced by an eddy-viscosity using the Boussinesq hypothesis[84], which is why functional models are also known as eddy-viscosity models. In the Boussinesq's hypothesis, the Reynolds stress tensor and the mean of the strain tensor is aligned. However, one characteristic of the functional model is that it totally ignores the backward energy cascade phenomenon, thus these kinds of models can be over dissipative. We can write the Reynold's stress tensor momentum transport considering only the deviatoric part of the as followed:

$$\tau_{ij}^{mod}\left(\tilde{U},\bar{\Delta}\right) = -2\nu_t^{mod}\left(S_{ij}\right) \qquad (4.26)$$

Here, S_{ij} is the strain rate tensor which can be written as, $S_{ij} = \frac{1}{2}(\frac{\partial U_i}{\partial x_j} + \frac{\partial U_j}{\partial x_i})$ and the term ν_t^{mod} is the eddy-viscosity term, which can be achieved from a specific model.

On the other hand, the eddy-diffusivity models are used to compute the density-velocity sub-grid term using the Prandtl number as state below:

$$\pi_{ij}^{mod}\left(\tilde{U},\phi,\bar{\Delta}\right) = -\frac{\nu_t^{mod}(g,d,\bar{\Delta})}{Pr_t} d_j \qquad (4.27)$$

Where, $d_j = \frac{\partial \phi}{\partial x_j}$, is a scalar gradient. The Prandtl number Pr=0.9, which is defined as effect of the momentum eddy-diffusivity relative to the eddy diffusivity of heat transfer.

For our thesis, we have picked the following eddy-viscosity models for performing the parametric study:

- AMD model[85]:

$$\nu_t^{AMD}(g,d,\bar{\Delta}) = C^{AMD}\frac{\max\left(0,-G_{ij}S_{ij}\right)}{g_{mn}g_{mn}} \qquad (4.28)$$

- AMD Scalar model[86]:

$$\nu_t^{AMD}(g,d,\bar{\Delta}) = C^{AMDs}\frac{\max\left(0,-D_j d_j\right)}{d_m d_m} \qquad (4.29)$$

- AMD model extended for cases with compressible flows[12]:
  This AMD model is an extension of the classical AMD model for compressible flow closure.

$$\nu_t^{AMD^c}(g,d,\bar{\Delta}) = C^{AMDc}\frac{\max\left(0,-\left(G_{ij}-G_{kk}I_{ij}\right)S_{ij}\right)}{\left(S_{mn}-\frac{1}{3}S_{kk}I_{mn}\right)S_{mn}} \qquad (4.30)$$

  The value of the functional model constants of each equation is 0.3.

4.3.2. Structural Models

The main purpose of the structural model is to approximate the sub-grid tensor, τ. It is done by the reconstruction of the filtered velocity. An alternative way of doing this is to perform a

formal series expansion. However, this method does not consider how the interaction of the sub-grid scales, and the resolved scales are in nature. The attempt to mathematically reconstruct the sub-grid term in an exact manner causes these kinds of models to have different approach compared to the functional models. Functional models use a similar eddy-viscosity and eddy-diffusivity term for every direction of the flow, but structural models do not have similar characteristics. Unlike the functional models, the structural models can consider the backward energy cascade process of the sub-grid scales dissipating energy back to the resolved scales. Thus, structural models are not over-dissipative like functional models. However, structural models often fail to properly estimate the energy production in the sub-grid scale compared to the functional models, hence they are often quite unstable in terms of running the simulations [87]. The following structural models were selected for the purpose of the parametric study:

- Gradient[74]:

$$\tau_{ij}^{grad} = \frac{1}{12} C^{grad} \bar{\Delta}_k^2 g_{ik} g_{jk} \qquad (4.31)$$

$$\pi_{ij}^{grad} = \frac{1}{12} C^{grad} \bar{\Delta}_k^2 g_{ik} d_k \qquad (4.32)$$

- Bardina[88]:

$$\tau_{ij}^{bard} = C^{bard} \left(\widetilde{U}_\iota \widetilde{U}_\jmath - \widehat{\widetilde{U}}_\iota \widehat{\widetilde{U}}_\jmath \right) \qquad (4.33)$$

$$\pi_{ij}^{bard} = C^{bard} \left(\widetilde{U}_\iota \tilde{T} - \hat{\tilde{T}} \widehat{\widetilde{U}}_\iota \right) \qquad (4.34)$$

- Scale Similarity [88]:

$$\tau_{ij}^{sim} = C^{sim} \left(\widehat{\widetilde{U}_\iota \widetilde{U}_\jmath} - \widehat{\widetilde{U}}_\iota \widehat{\widetilde{U}}_\jmath \right) \qquad (4.35)$$

$$\pi_{ij}^{sim} = C^{sim} \left(\widehat{\widetilde{U}_\jmath \tilde{\phi}} - \hat{\tilde{\phi}} \widehat{\widetilde{U}}_\jmath \right) \qquad (4.36)$$

- Scale Similarity for compressible flows [12]:

$$\tau_{ij}^{sim^c} = C^{sim^c} \left(\bar{\rho} \widehat{\widetilde{U}_\iota \widetilde{U}_\jmath} - \frac{\widehat{\bar{\rho} \widetilde{U}_\iota} \widehat{\bar{\rho} \widetilde{U}_\jmath}}{\bar{\rho}} \right) \qquad (4.37)$$

$$\pi_{ij}^{sim^c} = C^{sim^c} \left(\bar{\rho} \widehat{\tilde{\phi} \widetilde{U}_\jmath} - \frac{\widehat{\bar{\rho} \tilde{\phi}} \widehat{\bar{\rho} \widetilde{U}_\jmath}}{\bar{\rho}} \right) \qquad (4.38)$$

Here, the value of the constant term for all of the models above is 1.

4.3.3. Mixed Models

As we have previously discussed, both functional and structural models have their own advantages and disadvantages. To utilize the good characteristics of each model, using a mixed approach is a good way to cancel out the drawbacks. The functional models give better approximation of the interaction between the sub-grid and the resolved scales for energy transfer. However, the structural models give a better approximation on the structure of the sub-grid scale tensor, while also being able to give a good approximation of the anisotropic effects and other qualities like disequilibrium [89][90][53].

In this study, one functional mode has been tested, while the other models are two-layer mixed models combining the AMD, AMD scalar, AMD compressible functional models with structural models like Bardina, Gradient, Scale similarity model and Scale similarity model extended for compressible cases. One layer mode has not been used in this study, as David et al. [4] has already performed multiple one layer models. One-layer models usually uses a linear combination of between the functional and the structural models, whereas for two-layer models, the following equations is used:

$$\tau_{ij} = \alpha_1 \tau_{ij}^{fucn} + \beta_1 \tau_{ij}^{struc} \qquad (4.39)$$

$$\pi_{ij} = \alpha_2 \pi_{ij}^{fucn} + \beta_2 \pi_{ij}^{struc} \qquad (4.40)$$

Where, $\alpha_1, \alpha_2, \beta_1, \beta_2$ are all constants. Certain constant values can be picked to modulate the influence of functional and structural models to see which give better results.

The two layer model was further inspired by the work done by Streher et al. [24] where the constant of the models were properly modulated as the constant of the functional models decreases as the distance is increased from the wall position. The functional models can predict the characteristics of the flow better near the wall region; thus, this particular approach is quite beneficial. Also, the structural models predict the backscatter of the energy, thus compensating for the over-dissipative behavior of the functional models. Furthermore, the functional model is toned down at the center as the stresses associated with viscosity is less important in this region compared to the turbulent stresses, while structural models are better in approximating the turbulent stresses [12]. The equation for this approach is given in the following:

$$C_i^{func} = C^{func} + \left(0.5 + 0.5 tanh\left(\frac{y_i - s_c}{s_f}\right)\right)\left(C_c - C^{func}\right) \qquad (4.41)$$

Here, i indicates the index of the cell number in the direction normal to the wall, y indicates the distance from wall, s_c is the smoothing center, s_f is the smoothing factor, and the value C_c indicates the value of the constant at the center of the channel. These values were proposed by Streher et al. in their study [24].

5. Numerical Settings

For running the simulation, a software called TrioCFD [38] has been used which is an open-source code for performing computational fluid dynamics (CFD). This code was developed by French Alternative Energies and Atomic Energy Commission (CEA) and their Thermo-hydraulics and Fluid Mechanics department, for channel flow simulations [91][92][93][94][95][96][97][98], which is suitable for our case. The finite difference method was used to perform the calculations in a staggered mesh system, meaning that the information for scalar quantities are stored in the center of the cell and the vector quantities are stored at the cell faces[99]. In this thesis, we have used a method called finite difference method with meshes that has a staggered configuration, and the time derivatives are solved using a method called third order Runge-Kutta. Momentum conservation equations from the N-S equations were discretized using the fourth order discretization scheme and the mass equation were discretized using second order discretization scheme.

As mentioned in earlier chapter, the mesh must be generated using a hyperbolic tangent law stated below in the wall normal direction as the velocity and temperature gradient along this direction is quite high.

$$y_k = L_y\left(1+\frac{1}{a}tanh\left[\left(\frac{k-1}{N_y-1}-1\right)\tanh^{-1}(a)\right]\right), k \in [1, N_y] \qquad (5.1)$$

Here, a is called a mesh dilation parameter, whereas N_y indicates the grid point number along the wall normal direction of the channel flow. The other two directions, which are spanwise and streamwise direction have uniform meshing system. The filter size of the LES method depends on the mesh size as it was discussed in the chapter where LES filtering process has been described in detail. Thus, the size of the cell has a bigger influence on the simulation results. The mesh configuration chosen for this study has been provided on table. The mesh configuration of the DNS results that is going to be used as a reference to validate our data has also been included in the table.

Mesh name	Number of grid points N_x, N_y, N_z
DNS	1152x746x768
C	160x152x96

Table 5-1: Mesh configurations of the performed simulations.

Furthermore, since we are using LES models to study our case, we chose two different LES models to approximate the velocity-velocity and velocity-density sub-grid terms we get from momentum and energy conservation equations after applying the LES filtering. For the first

LES model, we chose a functional model named Anisotropic minimum dissipation (AMD) model extended for compressible cases introduced by Martin et al. [12] in his paper. This model is denoted by AMD^c (with constant term value of 0.3) and is used to calculate both sub-grid terms for the first case. This functional model was picked to validate our code with what Martin et al. [12] did in his paper, as he previously tested this model as well. For the second case, we chose a mixed model, which uses a combination of functional AMD model and structural Gradient model to calculate the velocity-velocity sub-grid term, where combination of AMD scalar model and Gradient model is used to calculate the velocity-density sub-grid term. Out of different ways to use mixed models, we have chosen a method presented by Streher et al. [24], which shows how tow layer mixed modeling can be used to consider AMD models more strongly near the wall region where the viscous stresses are more prominent, and slowly make the transition towards structural models where turbulent stresses are more prominent. The equation used to make this transition is given below:

$$C_i^{func} = C^{func} + \left(0.5 + 0.5tanh\left(\frac{y_i - s_c}{s_f}\right)\right)\left(C_c - C^{func}\right) \qquad (5.2)$$

Here, i indicates the index of the cell number in the direction normal to the wall, y indicates the distance from wall, s_c is the smoothing center, s_f is the smoothing factor, and the value C_c indicates the value of the constant at the center of the channel. We have chosen constant value of 0.6 for the AMD models, which will reach a value of 0.15 at the center of the channel by following the above equation as the distance from the wall increases. Detailed information of the simulation models is given in **table 5-2**.

Simulation name	Functional model		Structural Model		Type (cc)	Numerical Scheme	
	Name $\tau - \pi$	Constant $\tau - \pi$	Name $\tau - \pi$	Constant $\tau - \pi$		Momentum conv.	Mass conv.
Ac03-Ac03 (c4-c2)	AMD^c-AMD^c	0.3-0.3	x	x	1L	c4	c2
A06+G05-As06+G04 cc015 (c4-c2)	AMD-AMD^s	0.6-0.6	Grad-Grad	0.5-0.4	2L (0.15)	c4	c2

Table 5-2: Selected LES model for performing the parametric studies.

6. Results and Discussion

For the results, all of the data of the simulation were spatially averaged and later time averaged using the Ergodicity theorem [4]. The results are properly evaluated by comparing them with the DNS data with similar settings. The mean values, covariances and the cross correlations are checked in this thesis.

To perform a parametric study, the 1st order and 2nd order statistics are presented along with the result from the DNS data to visualize how much the LES models can predict the data accurately compared to the DNS data. Also, to compare the relative performance of the two LES models, the relative errors between the DNS data and the two LES model results are also presented. For each quantity of the T-LES models, the relative error has been calculated using the following equation[12]:

$$\varepsilon_X^{T-LES_j} = \frac{\sum_{i=1}^{N_y/2} log\left(\frac{y_i+1}{y_i}\right)\left|\left(X_i^{T-LES_j} - X_i^{DNS}\right)X_i^{T-LES_j}\right|}{\sum_{i=1}^{N_y} log\left(\frac{y_i+1}{y_i}\right)X_i^{DNS^2}} + \frac{\sum_{i=1}^{N_y/2} log\left(\frac{2\delta-y_{i+1}}{2\delta-y_i}\right)\left|\left(X_{N_y/2-i+1}^{T-LES_j} - X_{N_y/2-i+1}^{DNS}\right)X_{N_y/2-i+1}^{T-LES_j}\right|}{\sum_{i=1}^{N_y} log\left(\frac{2\delta-y_i}{2\delta-y_i}\right)X_i^{DNS^2}} \quad (6.1)$$

Where, X is the quantity that is being compared with the DNS data, T-LES$_j$ is the LES model for which the error is being calculated, ε is the relative error value between the LES model and the DNS data, y_i is the i-th point along the normal direction from the wall, δ is the half height of the channel where the flow is being investigated.

Later, the errors for any T-LES model were calculated for both mean (E_{mean}) and covariance (E_{rms}) quantities. The error is calculated by adding the errors obtained for all the values calculated by that T-LES model and then dividing the error with the sum of the worst error result obtained between all the T-LES models. The equations for the mean and covariance error calculation are given below:

$$Err_{mean}^{LES,j} = \frac{\sum_X \varepsilon_X^{LES,j}}{max\left(\sum_X \varepsilon_X^{LES,j}\right)} \quad (6.2)$$

Where, X= U, V, T and ϕ respectively. Similarly, for the covariances, we can write,

$$Err_{rms}^{LES,j} = \frac{\sum_X \varepsilon_X^{LES,j}}{max\left(\sum_X \varepsilon_X^{LES,j}\right)} \quad (6.3)$$

Where, X is the square root of the terms $\langle u'u'\rangle^{dev}$, $\langle v'v'\rangle^{dev}$, $\langle w'w'\rangle^{dev}$, $\langle \Theta'\Theta'\rangle^{dev}$, $\langle u'v'\rangle^{dev}$, $\langle u'\Theta'\rangle^{dev}$ and $\langle v'\Theta'\rangle^{dev}$. Using the values of the mean and covariance errors, we

later calculated the global error using the equation given below:

$$Err_{glob}^{LES,j} = \frac{nErr_{mean}^{LES,j} + mErr_{rms}^{LES,j}}{n+m} \qquad (6.4)$$

Where, the n and m are constant values that indicates the number of mean and covariance quantities considered for these calculations.

Note that, the subscripts "+" on every variable indicates normalized value of that variable with the following scaling: $x_i^+ = x_i U_\tau/\nu$, $U_i^+ = U_i/U_\tau$, $\theta_i^+ = |\theta_w - \theta|/\theta_\tau$,$\langle R_{ij}\rangle^+ = \langle R_{ij}\rangle/{U_\tau}^2$, $\langle U_i'\theta'\rangle^+ = \langle U_i'\theta'\rangle/(U_\tau\theta_\tau)$.

Where,

$U_\tau = \sqrt{\nu\partial U/\partial x_2}$=Friction velocity, $\theta_\tau = \phi_w/(\rho C_p U_\tau)$=Friction temperature, where ϕ_w is the heat flux for wall conduction, and θ_w= Wall temperature.

6.1. 1st order Statistics

Since the two models we picked have the same mesh configuration and discretization schemes, the only parametric study we performed here is to check which one of the two LES models gives us better approximation with respect to the DNS data. Note that the simulation results presented are preliminary results, as data were extracted while the simulations are not yet fully converged, but they are almost converged.

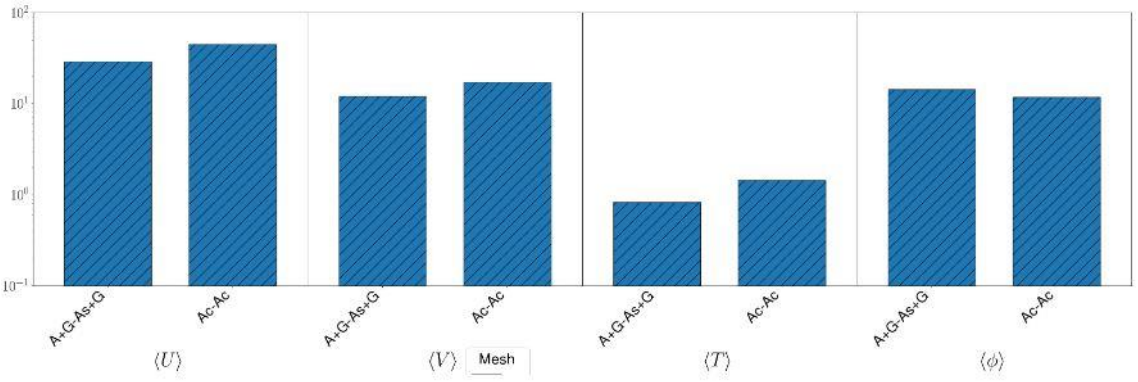

Figure 6.1: LES model error comparison of the mean quantities w.r.t DNS data.

One of the models is functional model, while the latter is a two-layer mixed model between functional and structural models, thus we can also get a better understanding on how having mixed model approach differentiates from a conventional functional model approach.

For the value of temperature, both the functional and mixed models give very good estimation, showing an error near to 1%. In **figure 6.1** the mixed models are more accurate

compared to the DNS data, excluding the heat flux values. The heat flux error for a mixed model was also higher for C mesh configuration compared to Ac03-Ac03 model, which was presented by Martin et al. [12] in his paper. So far, we can conclude from the preliminary simulation data that the mixed model is an overall improvement over the functional model that we picked.

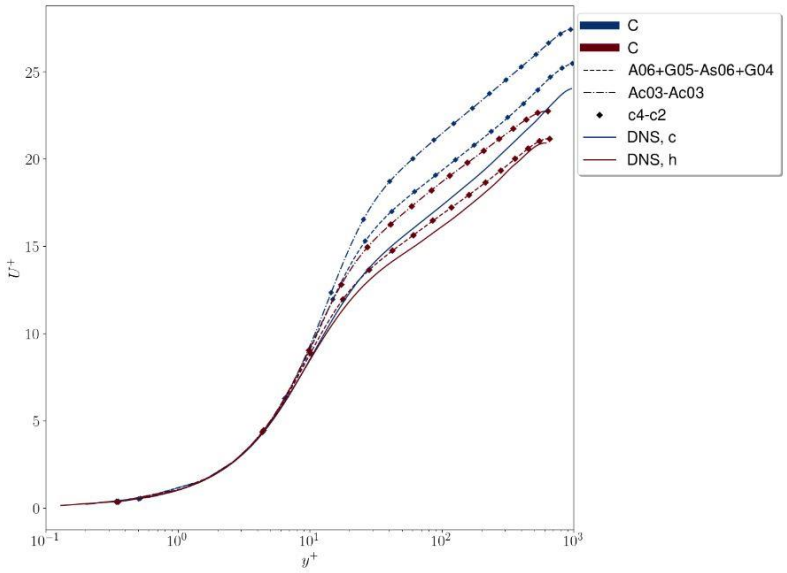

Figure 6.2: Normalized streamwise velocity profiles as a function of the distance from the hot and cold walls.

In the first order statistics profiles, the mean quantities are measured and compared in logarithmic scale. In **figure 6.2**, we can see the mean streamwise velocity for both the hot and cold wall. As it can be noticed, both models are well approximated for $y^+<10$, which is the buffer layer region. However, at further distances from the wall, it can be seen the both the models diverge from the DNS results, while the functional model diverges the furthest for both the hot and cold walls. Both models overestimate the profiles for both hot and cold wall, but the mixed model gives far better approximation and is much closer to the DNS profiles.

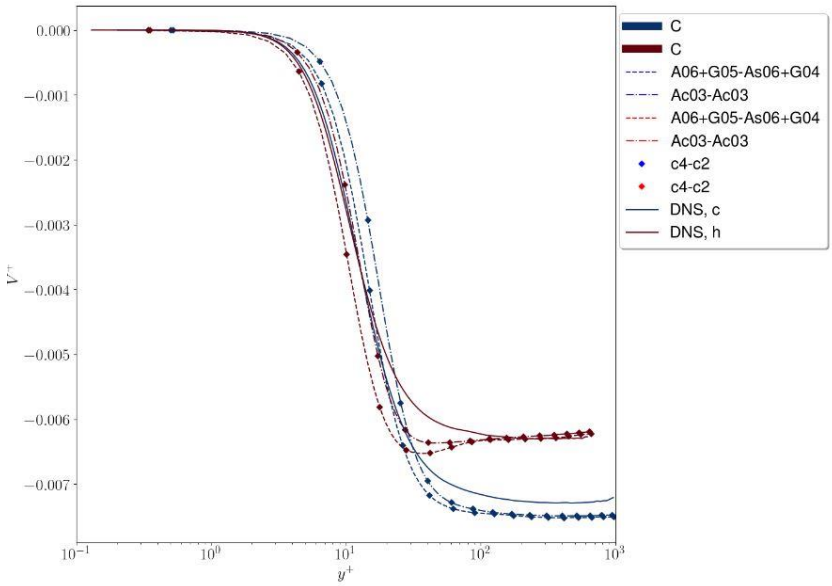

Figure 6.3: Normalized wall-normal velocity profiles as a function of the distance from the hot and cold walls.

For the wall normal velocity, the trends are much closer to the DNS data compared to the streamwise velocity. A probable explanation for this is the fact that this term is included in the energy conservation equation. However, like the streamwise velocity, the AMD^c model slightly overestimates both hot and cold wall profiles for the majority of the distance, whereas the mixed model slightly underestimates the hot wall profile. However, the cold wall profile is well approximated by the mixed model before $y^+<13$, but later it underestimates.

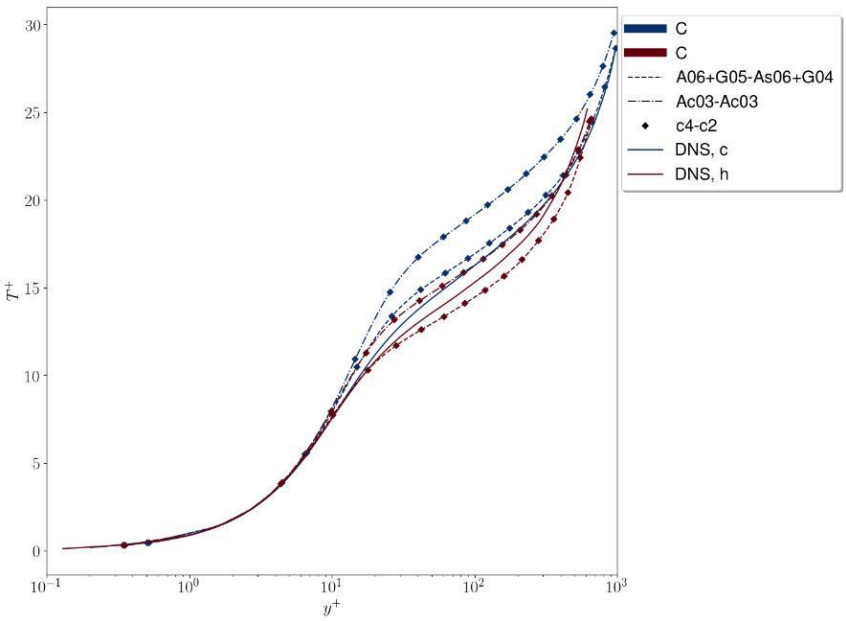

Figure 6.4: Normalized temperature profiles as a function of the distance from the hot and cold walls.

For the temperature profile, again the mixed model gives good cold wall temperature approximation but underestimates the hot wall temperature profile. The AMD^c overestimates for both cases.

6.2. 2nd order statistics

For the second order statistics, it can be noticed that the error of the velocity cross-correlations for mixed model is slightly higher than the functional model. This phenomenon is also observed in the LES results of Martin et al [12]. However, this term is well approximated by both models, probably because of the involvement of this term in the momentum conservation equation.

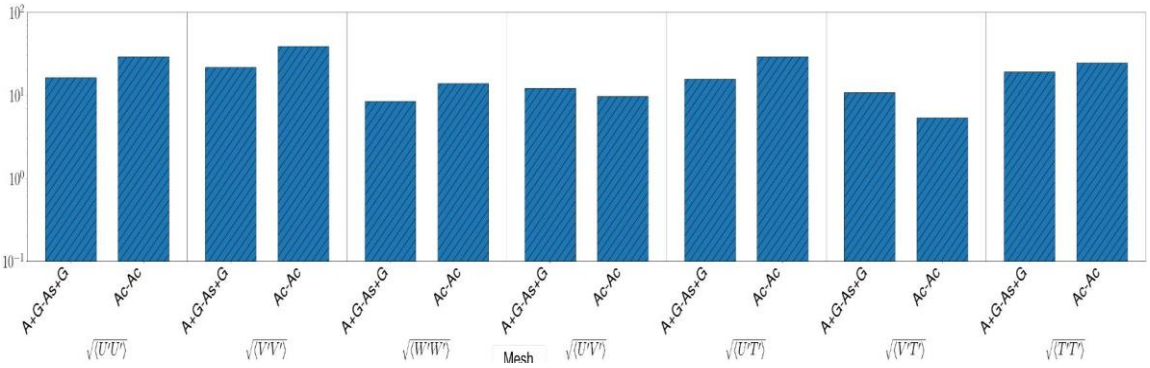

Figure 6.5: LES model error comparison of the correlations w.r.t DNS data.

For all the diagonal terms of the Reynolds stress tensor, the mixed model is an improvement over the functional model as it utilized both the over-dissipative (AMD) and under-dissipative behavior (Gradient) of the mixed model.

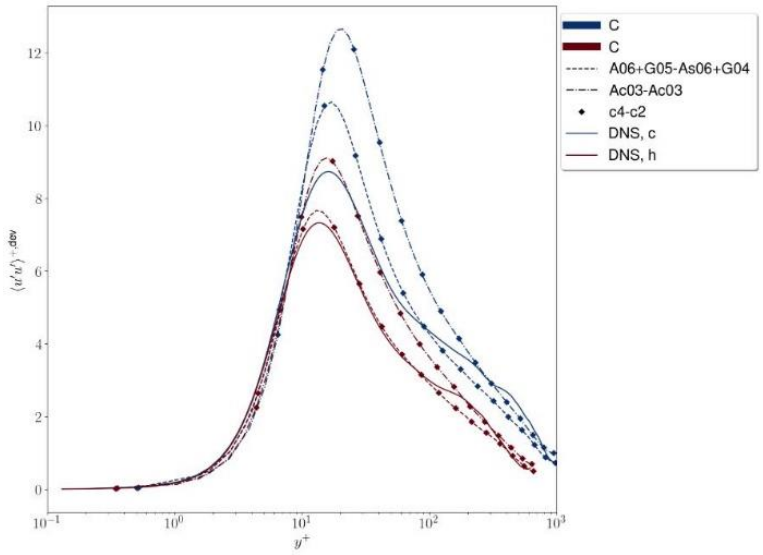

Figure 6.6: The streamwise velocity correlation profiles.

The profiles of the second order statistics also presents valuable insights on how the profiles are estimating the results compared to the DNS values and which region from the wall is giving better results and where there are still further improvements are required.

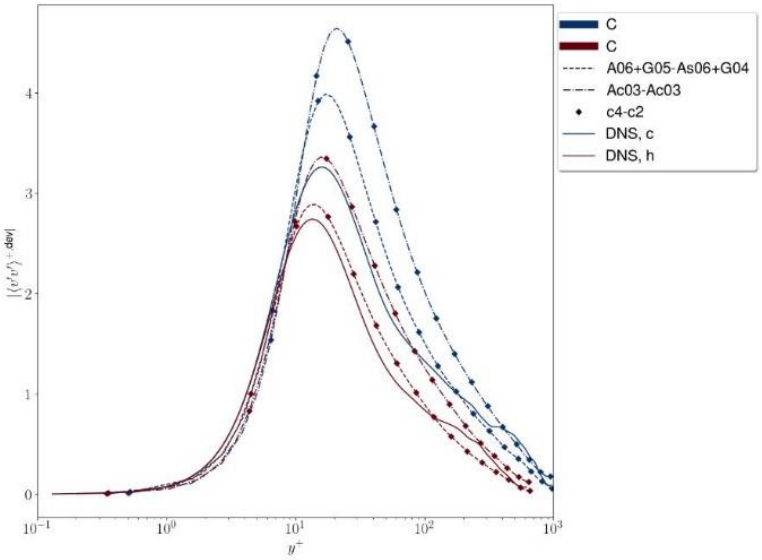

Figure 6.7: The wall-normal velocity correlation profiles.

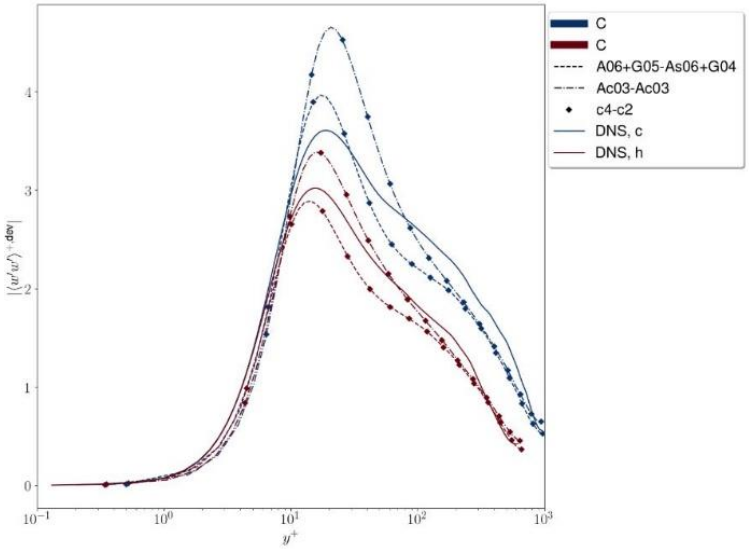

Figure 6.8: The spanwise velocity correlation profiles.

For all the velocity correlations, there is a peak that can be observed around y^+=13 in DNS data, however, this peak is heavily overestimated by the functional model and overestimated by the mixed model, but mixed model is a clear improvement. Also, we noticed that the quasi-plateau around y^+=100 for DNS results due to the effects of high Reynolds number is not reproduced properly by the AMD model, but rather the mixed model approximates it slightly better than the AMD model.

For the velocity cross-correlation, we can see that both models give a good approximation of the profiles for both cold and hot walls.

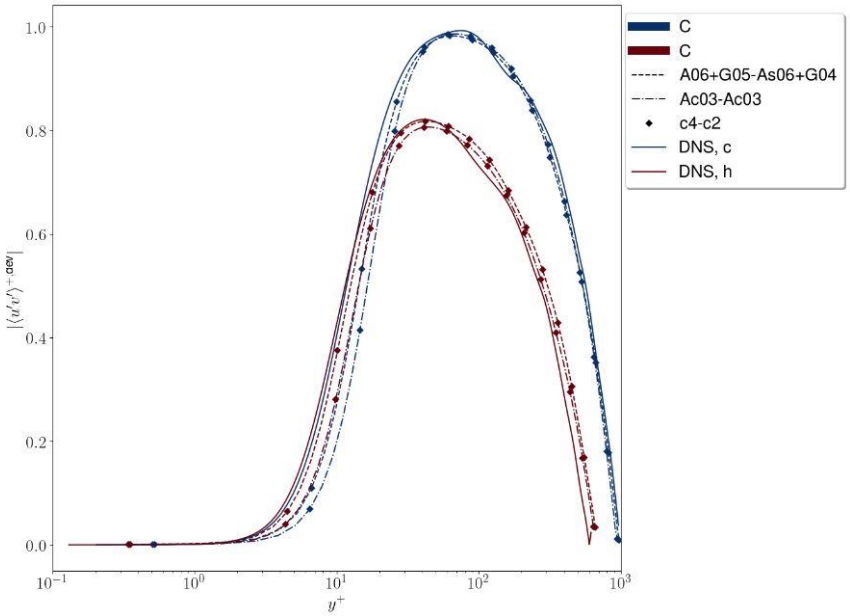

Figure 6.9: The velocity cross-correlation profiles for streamwise and wall normal velocities.

For the temperature correlation <u'Θ'>, the trend is somewhat similar to the velocity correlations, where the functional model overestimates the plots. The mixed model gives better approximation, but for the hot wall, it slightly underestimates after the peak region.

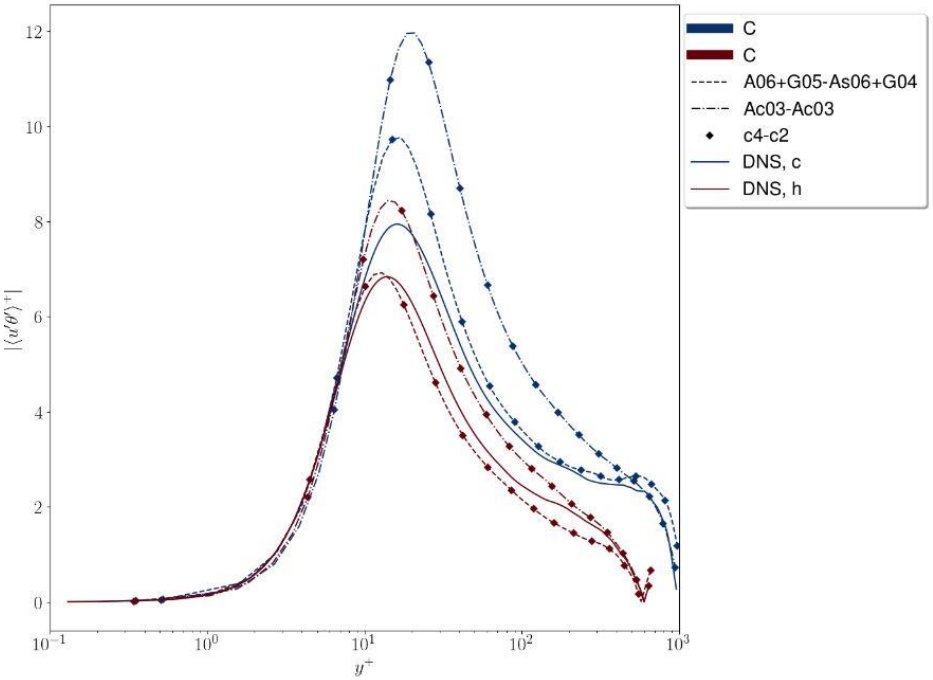

Figure 6.10: The streamwise velocity-temperature correlation profiles.

The wall normal velocity and temperature correlation <v'Θ'> gives better approximation for both models as we can see in **figure 6.11**, thus the error for this term is also lower for both simulations.

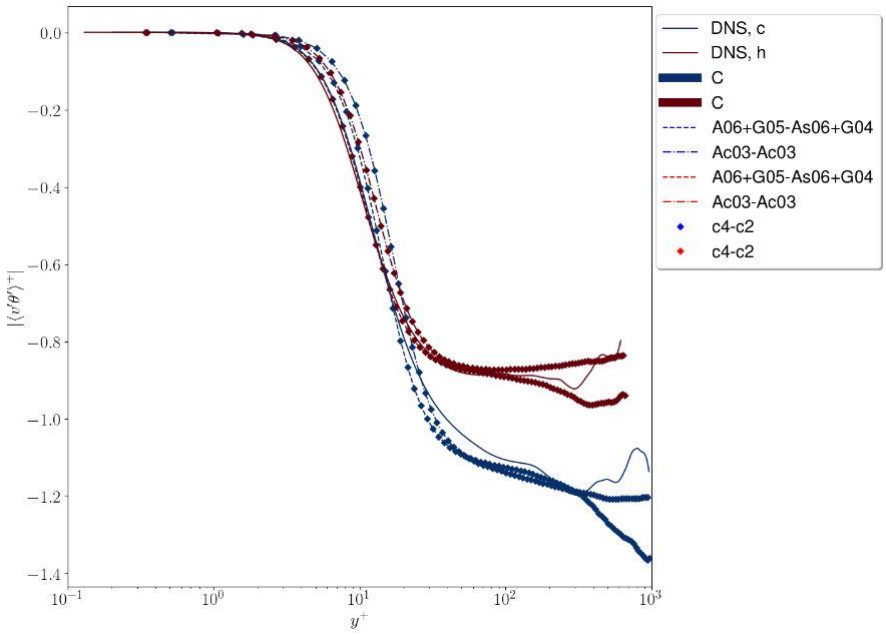

Figure 6.11: The wall normal velocity-temperature correlation profiles.

The temperature auto-correlations are poorly approximated as in can be seen in **figure 6.12**. This kind of performance may be attributed to the fact that there are no proper models associated for temperature correlations, thus the sub-grid terms are poorly estimated.

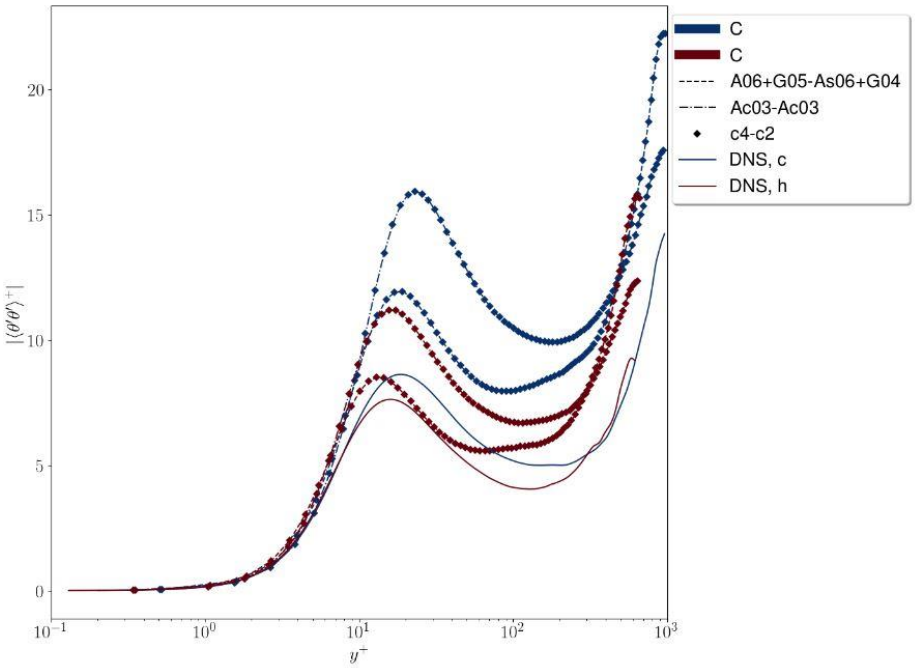

Figure 6.12: Temperature correlation profiles.

6.3. General assessment results of the LES models

Here, **figure 6.13** shows the relative error of the mean quantities and correlation quantities, while **figure 6.14** shows global relative error respectively. From the error comparison we have seen from the previous section, it was evident that for most cases, the mixed model approximates the quantities better than the conventional functional models.

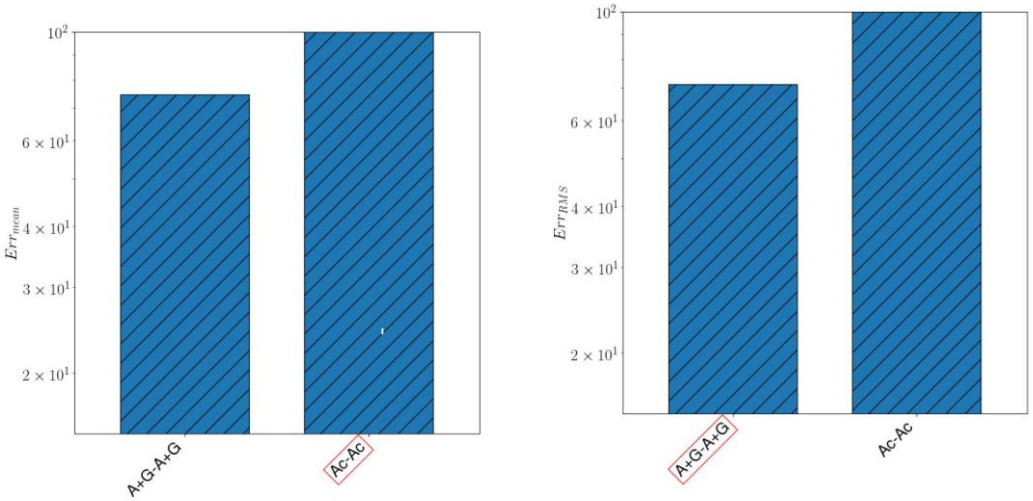

Figure 6.13: The relation errors for mean and rms quantities.

Thus, the relative error for mean, correlation quantities and the global relative error is clearly lower for the mixed models, which indicates that it definitely offers an improvement over the functional model.

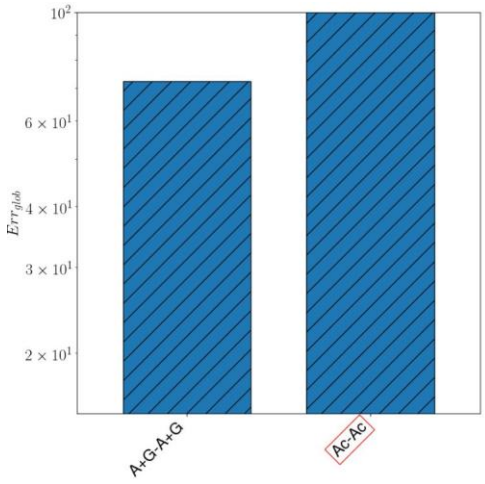

Figure 6.14: The relative global error for the LES models.

7. Conclusion

For this study, two different T-LES models were investigated for a specific mesh configuration and thermal flux values for channel flow of pressurized air in the solar receiver. The flow was highly anisothermal as the two opposite walls of the channel flow had different temperatures, but both were at really high temperatures, thus heating the channel flow from both sides of the wall. The aim of the study was to investigate whether the two layered mixed model provides a better approximation of the mean and correlation quantities when compared with the DNS data with similar settings. To confirm whether the simulation is giving reasonable results, one of the functional method LES simulations from Martin et al. [12] using compressible AMD model for fourth order discretization of the momentum equation and second order discretization for the mass conservation was reproduced. Later, a mixed model using the combination of AMD and Gradient model using similar discretization schemes as the AMD model was simulated. It was noticed that for the mean quantities, the mixed model gave better approximation. For correlations, the mixed models also gave better results. Also, it was noticed from the generated profiles that the peaks of the correlations were better approximated by the mixed model as well.

In future, more combinations of functional and mixed models can be investigated. Furthermore, different meshing configurations can be investigated to perform a mesh sensitivity test to check whether the estimation of the results improve further or not, along with different thermal conditions to check the effects of the thermal conditions on the simulation results to better understand the dynamic between the temperature and the velocity of the flow.

8. Future Activities

For future activities as part of an internship under the part of the SOLAIRE ANR project in collaboration with PROMES-CNRS and LISN lab, the following simulations listed on **table 8-1** are going to be performed in a similar manner.

Simulation name	Functional model		Structural Model		Type	Numerical Scheme	
	Name	Constant	Name	Constant		Momentum conv.	Mass conv.
A03-As03	AMD-AMD^s	0.3-0.3	x	x	1L	c4	c2
A06+B05-As06+B04 cc015	AMD-AMD^s	0.6-0.6	Bard-Bard	0.5-0.4	2L (0.15)	c2	c2
A06+B05-As06+B04 cc015	AMD-AMD^s	0.6-0.6	Bard-Bard	0.5-0.4	2L (0.15)	c4	c2
A06+Sc05-As06+S04 cc015	AMD-AMD^s	0.6-0.6	Sim^c-Sim	0.5-0.4	2L (0.15)	c4	c2
A06+G05-A06+G04 cc015	AMD-AMD	0.6-0.6	Grad-Grad	0.5-0.4	2L (0.15)	c2	c2
A06+G05-A06+G04 cc015	AMD-AMD	0.6-0.6	Grad-Grad	0.5-0.4	2L (0.15)	c4	c2
A06+G05-As06+G04 cc015	AMD-AMD^s	0.6-0.6	Grad-Grad	0.5-0.4	2L (0.15)	c4	c2

Table 8-1: Selected LES model configurations to be simulated in the future.

The simulations will include one simulation having AMD and AMD scalar functional models to simulate the results for the same physical and numerical settings. The other six simulation

setup includes two layered mixed models having AMD, AMD scalar as functional models and Bardina, Gradient, Scale similarity and Compressible Scale similarity as structural models.

Thermal Condition name	Heat sink (MW/m^3)	Hot wall heat flux (KW/m^2)	Cold wall heat flux (KW/m^2)
S0	0	98	-98
S4	164	587	410

Table 8-2: The selected thermal conditions for testing the effects of the heat fluxes at different locations of the channel flow.

To further the study and have a better parametric understanding of the simulations, two settings of thermal conditions (see **table 8-2**) and three different sets of mesh configuration (see **table 8-3**) are going to be considered. Furthermore, different discretization schemes for same mixed models are also considered. At the end of the study, it is expected to realize the full understanding of the mesh sensitivity, the effect of the thermal conditions and discretization schemes on the results of the LES simulation so that we can understand which of the simulations give us better results by comparing them with DNS and each other.

Mesh name	Number of grid points N_x, N_y, N_z
A	256x152x192
B	192x152x128
C	160x152x96

Table 8-3: The selected mesh configurations to perform mesh sensitivity.

9. Acknowledgements

I would like to gratefully acknowledge the CEA, where the TRUST platform was developed for the established of the TrioCFD code. I would also like to acknowledge the opportunity provided by by Dr. Adrien TOUTANT and Yanis Zatout, to work under the SOLAIRE ANR project, which is working on the application of pressurized air on solar receivers for achieving high-efficiency centralized solar power plants. I would also like to thank my academic supervisor Dr. Carlos David Perez Segarra for his invaluable support, encouragement and guidance during my thesis.

10. Bibliography

[1] IEA, “Renewables, Energy system overview,” *IEA Renewables,* 2022. https://www.iea.org/reports/renewables.

[2] “The key figures of energy in the world,” Sep. 26, 2017.

[3] IEA, “Technology Roadmap - Concentrating Solar Power,” Paris, 2010. [Online]. Available: https://www.iea.org/reports/technology-roadmap-concentrating-solar-power.

[4] M. David, “Simulation et modélisation des écoulements dans les récepteurs solaires à gaz sous-pression To cite this version : HAL Id : tel-03574288,” 2022.

[5] IREA, *Renewable Power Generation Costs in 2020*. 2020.

[6] A. Caraballo, S. Galán-Casado, Á. Caballero, and S. Serena, “Molten Salts for Sensible Thermal Energy Storage: A Review and an Energy Performance Analysis,” *Energies*, vol. 14, no. 4, p. 1197, Feb. 2021, doi: 10.3390/en14041197.

[7] G. Flamant *et al.*, “A New Heat Transfer Fluid for Concentrating Solar Systems: Particle Flow in Tubes,” *Energy Procedia*, vol. 49, pp. 617–626, 2014, doi: 10.1016/j.egypro.2014.03.067.

[8] C. K. Ho, “Advances in central receivers for concentrating solar applications,” *Sol. Energy*, vol. 152, pp. 38–56, Aug. 2017, doi: 10.1016/j.solener.2017.03.048.

[9] J. Pacio, A. Fritsch, C. Singer, and R. Uhlig, “Liquid Metals as Efficient Coolants for High-intensity Point-focus Receivers: Implications to the Design and Performance of Next-generation CSP Systems,” *Energy Procedia*, vol. 49, pp. 647–655, 2014, doi: 10.1016/j.egypro.2014.03.070.

[10] M. Sedighi *et al.*, “Design of high-temperature atmospheric and pressurised gas-phase solar receivers: A comprehensive review on numerical modelling and performance parameters,” *Sol. Energy*, vol. 201, pp. 701–723, May 2020, doi: 10.1016/j.solener.2020.03.025.

[11] Y. Zhou, “Turbulence theories and statistical closure approaches,” *Phys. Rep.*, vol. 935, pp. 1–117, Nov. 2021, doi: 10.1016/j.physrep.2021.07.001.

[12] M. David, A. Toutant, and F. Bataille, “Thermal large-eddy simulation methods to model highly anisothermal and turbulent flows,” *Phys. Fluids*, vol. 35, no. 3, 2023, doi: 10.1063/5.0139433.

[13] H. J. Kull, “Theory of the Rayleigh-Taylor instability,” *Phys. Rep.*, vol. 206, no. 5, pp. 197–325, Aug. 1991, doi: 10.1016/0370-1573(91)90153-D.

[14] Y. Zhou, “Rayleigh–Taylor and Richtmyer–Meshkov instability induced flow, turbulence, and mixing. I,” *Phys. Rep.*, vol. 720–722, pp. 1–136, Dec. 2017, doi: 10.1016/j.physrep.2017.07.005.

[15] S.-H. Peng and L. Davidson, “On a subgrid-scale heat flux model for large eddy simulation of turbulent thermal flow,” *Int. J. Heat Mass Transf.*, vol. 45, no. 7, pp.

1393–1405, Mar. 2002, doi: 10.1016/S0017-9310(01)00254-X.

[16] C. W. Higgins, M. B. Parlange, and C. Meneveau, “The heat flux and the temperature gradient in the lower atmosphere,” *Geophys. Res. Lett.*, vol. 31, no. 22, Nov. 2004, doi: 10.1029/2004GL020053.

[17] J. SMAGORINSKY, “GENERAL CIRCULATION EXPERIMENTS WITH THE PRIMITIVE EQUATIONS,” *Mon. Weather Rev.*, vol. 91, no. 3, pp. 99–164, Mar. 1963, doi: 10.1175/1520-0493(1963)091<0099:GCEWTP>2.3.CO;2.

[18] A. Leonard and A. Leonard, “Large-eddy simulation of chaotic convection and beyond,” Jan. 1997, doi: 10.2514/6.1997-204.

[19] B.-C. WANG, E. YEE, D. J. BERGSTROM, and O. IIDA, “New dynamic subgrid-scale heat flux models for large-eddy simulation of thermal convection based on the general gradient diffusion hypothesis,” *J. Fluid Mech.*, vol. 604, pp. 125–163, Jun. 2008, doi: 10.1017/S0022112008001079.

[20] V. C. Wong and D. K. Lilly, “A comparison of two dynamic subgrid closure methods for turbulent thermal convection,” *Phys. Fluids*, vol. 6, no. 2, pp. 1016–1023, Feb. 1994, doi: 10.1063/1.868335.

[21] B. Vreman, B. Geurts, and H. Kuerten, “On the formulation of the dynamic mixed subgrid-scale model,” *Phys. Fluids*, vol. 6, no. 12, pp. 4057–4059, Dec. 1994, doi: 10.1063/1.868333.

[22] K. Horiuti, “A new dynamic two-parameter mixed model for large-eddy simulation,” *Phys. Fluids*, vol. 9, no. 11, pp. 3443–3464, Nov. 1997, doi: 10.1063/1.869454.

[23] G. S. Winckelmans, A. A. Wray, O. V. Vasilyev, and H. Jeanmart, “Explicit-filtering large-eddy simulation using the tensor-diffusivity model supplemented by a dynamic Smagorinsky term,” *Phys. Fluids*, vol. 13, no. 5, pp. 1385–1403, May 2001, doi: 10.1063/1.1360192.

[24] L. B. Streher, M. H. Silvis, P. Cifani, and R. W. C. P. Verstappen, “Mixed modeling for large-eddy simulation: The single-layer and two-layer minimum-dissipation-Bardina models,” *AIP Adv.*, vol. 11, no. 1, 2021, doi: 10.1063/5.0015293.

[25] B. J. Geurts, A. Rouhi, and U. Piomelli, “Recent progress on reliability assessment of large-eddy simulation,” *J. Fluids Struct.*, vol. 91, p. 102615, Nov. 2019, doi: 10.1016/j.jfluidstructs.2019.03.008.

[26] J. Meyers, B. J. Geurts, and P. Sagaut, “A computational error-assessment of central finite-volume discretizations in large-eddy simulation using a Smagorinsky model,” *J. Comput. Phys.*, vol. 227, no. 1, pp. 156–173, Nov. 2007, doi: 10.1016/j.jcp.2007.07.012.

[27] S. Singh, D. You, and S. T. Bose, “Large-eddy simulation of turbulent channel flow using explicit filtering and dynamic mixed models,” *Phys. Fluids*, vol. 24, no. 8, p. 085105, Aug. 2012, doi: 10.1063/1.4745007.

[28] H. Goldstein, C. Poole, J. Safko, and S. R. Addison, “Classical Mechanics, 3rd ed.,” *Am. J. Phys.*, vol. 70, no. 7, pp. 782–783, Jul. 2002, doi: 10.1119/1.1484149.

[29] I. Newton, *Sir Isaac Newton's Mathematical principles of natural philosophy, and his System of the world*. Berkeley: University of California Press, 1962.

[30] R. Clausius, "Ueber die bewegende Kraft der Wärme und die Gesetze, welche sich daraus für die Wärmelehre selbst ableiten lassen," *Ann. der Phys. und Chemie*, vol. 155, no. 3, pp. 368–397, 1850, doi: 10.1002/andp.18501550306.

[31] J. Fourier, "No TitleMémoire Sur La Propagation de La Chaleur Dans Les Corps Solides. Nouveau Bulletin des Sciences de la Société Philomathique de Paris," 1807.

[32] E. Garnier, N. Adams, and P. Sagaut, "Compressible Turbulence Dynamics," 2009, pp. 41–76.

[33] E. Clapeyron, "Memoire Sur La Puissance Motrice de La Chaleur," *J. l'Ecole Polytech.*, pp. 153–190, 1893.

[34] W. Sutherland, "LII. The viscosity of gases and molecular force," *London, Edinburgh, Dublin Philos. Mag. J. Sci.*, vol. 36, no. 223, pp. 507–531, Dec. 1893, doi: 10.1080/14786449308620508.

[35] S. Paolucci, "On the Filtering of Sound from the Navier–Stokes Equations," *NASA STI/Recon Tech. Rep.*, 1982, doi: https://www.researchgate.net/publication/234227502_On_the_Filtering_of_Sound_from_the_Navier-Stokes_Equations.

[36] J. Salat, S. Xin, P. Joubert, A. Sergent, F. Penot, and P. Le Quéré, "Experimental and numerical investigation of turbulent natural convection in a large air-filled cavity," *Int. J. Heat Fluid Flow*, vol. 25, no. 5, pp. 824–832, Oct. 2004, doi: 10.1016/j.ijheatfluidflow.2004.04.003.

[37] S. Xin, P. Le Quéré, and O. Daube, "Natural convection in a differentially heated horizontal cylinder: Effects of Prandtl number on flow structure and instability," *Phys. Fluids*, vol. 9, no. 4, pp. 1014–1033, Apr. 1997, doi: 10.1063/1.869197.

[38] C. Calvin, O. Cueto, and P. Emonot, "An object-oriented approach to the design of fluid mechanics software," *ESAIM Math. Model. Numer. Anal.*, vol. 36, no. 5, pp. 907–921, Sep. 2002, doi: 10.1051/m2an:2002038.

[39] A. M. Jaffe, "The millennium grand challenge in mathematics," *Not. Am. Math. Soc.*, vol. 53, no. 6, 2006.

[40] J. Leray, "Sur le mouvement d'un liquide visqueux emplissant l'espace," *Acta Math.*, vol. 63, pp. 193–248, 1934, doi: 10.1007/BF02547354.

[41] C. Bailly and G. Comte-Bellot, *Turbulence*. Cham: Springer International Publishing, 2015.

[42] C.-W. Tsang and C. Rutland, "Effects of Numerical Schemes on Large Eddy Simulation of Turbulent Planar Gas Jet and Diesel Spray," *SAE Int. J. Fuels Lubr.*, vol. 9, no. 1, pp. 2016-01–0866, Apr. 2016, doi: 10.4271/2016-01-0866.

[43] N. N. Mansour, P. Moin, W. C. Reynolds, and J. H. Ferziger, "Improved Methods for Large Eddy Simulations of Turbulence," in *Turbulent Shear Flows I*, Berlin,

Heidelberg: Springer Berlin Heidelberg, 1979, pp. 386–401.

[44] F. Gao and E. E. O'Brien, "A large-eddy simulation scheme for turbulent reacting flows," *Phys. Fluids A Fluid Dyn.*, vol. 5, no. 6, pp. 1282–1284, Jun. 1993, doi: 10.1063/1.858617.

[45] B. VREMAN, B. GEURTS, and H. KUERTEN, "COMPARISION OF NUMERICAL SCHEMES IN LARGE-EDDY SIMULATION OF THE TEMPORAL MIXING LAYER," *Int. J. Numer. Methods Fluids*, vol. 22, no. 4, pp. 297–311, Feb. 1996, doi: 10.1002/(SICI)1097-0363(19960229)22:4<297::AID-FLD361>3.0.CO;2-X.

[46] P. Lenaers, P. Schlatter, G. Brethouwer, and A. V. Johansson, "A new high-order method for the simulation of incompressible wall-bounded turbulent flows," *J. Comput. Phys.*, vol. 272, pp. 108–126, Sep. 2014, doi: 10.1016/j.jcp.2014.04.034.

[47] R. Vinuesa, C. Prus, P. Schlatter, and H. M. Nagib, "Convergence of numerical simulations of turbulent wall-bounded flows and mean cross-flow structure of rectangular ducts," *Meccanica*, vol. 51, no. 12, pp. 3025–3042, Dec. 2016, doi: 10.1007/s11012-016-0558-0.

[48] R. Courant, K. Friedrichs, and H. Lewy, "On the Partial Difference Equations of Mathematical Physics," *IBM J. Res. Dev.*, vol. 11, no. 2, pp. 215–234, Mar. 1967, doi: 10.1147/rd.112.0215.

[49] P. C. Marcel Lesieur, Olivier Métais, *Large-eddy simulations of turbulence*. Cambridge University Press, 2005.

[50] P. Sagaut, and Y.-T. Lee, "Large Eddy Simulation for Incompressible Flows: An Introduction. Scientific Computation Series," *Appl. Mech. Rev.*, vol. 55, no. 6, pp. B115–B116, Nov. 2002, doi: 10.1115/1.1508154.

[51] W. J. L. Luigi C. Berselli, Traian Iliescu, *Mathematics of Large Eddy Simulation of Turbulent Flows*. Berlin/Heidelberg: Springer-Verlag, 2006.

[52] B. P. Leonard, "A stable and accurate convective modelling procedure based on quadratic upstream interpolation," *Comput. Methods Appl. Mech. Eng.*, vol. 19, no. 1, pp. 59–98, Jun. 1979, doi: 10.1016/0045-7825(79)90034-3.

[53] U. Piomelli, G. N. Coleman, and J. Kim, "On the effects of nonequilibrium on the subgrid-scale stresses," *Phys. Fluids*, vol. 9, no. 9, pp. 2740–2748, Sep. 1997, doi: 10.1063/1.869385.

[54] H. K. Moffatt, " Turbulence and Stochastic Processes: Kolmogorov's Ideas 50 Years On . Edited by J. C. R. H UNT , O. M. P HILLIPS and D. W ILLIAMS . Proceedings of the Royal Society, London , A, vol. 434, 1991, pp. 1–240. £19.50 ," *J. Fluid Mech.*, vol. 275, no. 1890, pp. 406–408, 1994, doi: 10.1017/s0022112094212417.

[55] N. A. Adams and S. Hickel, "Implicit Large-Eddy Simulation: Theory and Application," 2009, pp. 743–750.

[56] F. K. Chow and P. Moin, "A further study of numerical errors in large-eddy simulations," *J. Comput. Phys.*, vol. 184, no. 2, pp. 366–380, Jan. 2003, doi: 10.1016/S0021-9991(02)00020-7.

[57] J. Meyers, B. J. Geurts, and M. Baelmans, “Database analysis of errors in large-eddy simulation,” *Phys. Fluids*, vol. 15, no. 9, pp. 2740–2755, Sep. 2003, doi: 10.1063/1.1597683.

[58] B. J. Geurts, “Analysis of errors occurring in large eddy simulation,” *Philos. Trans. R. Soc. A Math. Phys. Eng. Sci.*, vol. 367, no. 1899, pp. 2873–2883, Jul. 2009, doi: 10.1098/rsta.2009.0001.

[59] A. Lozano-Durán and H. J. Bae, “Error scaling of large-eddy simulation in the outer region of wall-bounded turbulence,” *J. Comput. Phys.*, vol. 392, pp. 532–555, Sep. 2019, doi: 10.1016/j.jcp.2019.04.063.

[60] D. Carati and A. A. Wray, “Time filtering in large eddy simulation,” *Proc. summer Progr.*, vol. 2000, pp. 263–270, 2000.

[61] P. Sagaut, “On the use of time-dependent filters for large-eddy simulation,” *ESAIM Proc.*, vol. 10, pp. 1–7, Aug. 2001, doi: 10.1051/proc:2001015.

[62] F. van der Bos and B. J. Geurts, “Commutator errors in the filtering approach to large-eddy simulation,” *Phys. Fluids*, vol. 17, no. 3, p. 035108, Mar. 2005, doi: 10.1063/1.1852579.

[63] P. Durbin, “Turbulent Flows. By S. B. P OPE . Cambridge University Press, 2000. 771 pp. ISBN 0 521 59886 9. £29.95 or $49.95 (paperback); ISBN 0 521 59125 2. £80.00 or $130.00 (hardback).,” *J. Fluid Mech.*, vol. 427, pp. 410–411, Jan. 2001, doi: 10.1017/S0022112000212913.

[64] T. S. Lund, “The use of explicit filters in large eddy simulation,” *Comput. Math. with Appl.*, vol. 46, no. 4, pp. 603–616, Aug. 2003, doi: 10.1016/S0898-1221(03)90019-8.

[65] J. Mathew, R. Lechner, H. Foysi, J. Sesterhenn, and R. Friedrich, “An explicit filtering method for large eddy simulation of compressible flows,” *Phys. Fluids*, vol. 15, no. 8, pp. 2279–2289, Aug. 2003, doi: 10.1063/1.1586271.

[66] S. T. Bose, P. Moin, and D. You, “Grid-independent large-eddy simulation using explicit filtering,” *Phys. Fluids*, vol. 22, no. 10, p. 105103, Oct. 2010, doi: 10.1063/1.3485774.

[67] P. J. Mason and N. S. Callen, “On the magnitude of the subgrid-scale eddy coefficient in large-eddy simulations of turbulent channel flow,” *J. Fluid Mech.*, vol. 162, no. 1, p. 439, Jan. 1986, doi: 10.1017/S0022112086002112.

[68] S. Ghosal, “An Analysis of Numerical Errors in Large-Eddy Simulations of Turbulence,” *J. Comput. Phys.*, vol. 125, no. 1, pp. 187–206, Apr. 1996, doi: 10.1006/jcph.1996.0088.

[69] A. Muschinski, “A similarity theory of locally homogeneous and isotropic turbulence generated by a Smagorinsky-type LES,” *J. Fluid Mech.*, vol. 325, pp. 239–260, Oct. 1996, doi: 10.1017/S0022112096008105.

[70] N. Park, J. Y. Yoo, and H. Choi, “Discretization errors in large eddy simulation: on the suitability of centered and upwind-biased compact difference schemes,” *J. Comput. Phys.*, vol. 198, no. 2, pp. 580–616, Aug. 2004, doi:

10.1016/j.jcp.2004.01.017.

[71] M. Lesieur and P. Comte, “Favre filtering and macro-temperature in large-eddy simulations of compressible turbulence,” *Comptes Rendus l’Académie des Sci. - Ser. IIB - Mech.*, vol. 329, no. 5, pp. 363–368, May 2001, doi: 10.1016/S1620-7742(01)01331-9.

[72] A. J. Favre, “the Equations of Compressible Turbulent Gases,” *Null*, 1965.

[73] A. Favre, “Turbulence: Space-time statistical properties and behavior in supersonic flows,” *Phys. Fluids*, vol. 26, no. 10, p. 2851, 1983, doi: 10.1063/1.864049.

[74] A. Leonard, “Energy Cascade in Large-Eddy Simulations of Turbulent Fluid Flows,” 1975, pp. 237–248.

[75] S. Ghosal and P. Moin, “The Basic Equations for the Large Eddy Simulation of Turbulent Flows in Complex Geometry,” *J. Comput. Phys.*, vol. 118, no. 1, pp. 24–37, Apr. 1995, doi: 10.1006/jcph.1995.1077.

[76] O. V. Vasilyev, T. S. Lund, and P. Moin, “A General Class of Commutative Filters for LES in Complex Geometries,” *J. Comput. Phys.*, vol. 146, no. 1, pp. 82–104, Oct. 1998, doi: 10.1006/jcph.1998.6060.

[77] D. Razafindralandy, A. Hamdouni, and M. Oberlack, “Analysis and development of subgrid turbulence models preserving the symmetry properties of the Navier–Stokes equations,” *Eur. J. Mech. - B/Fluids*, vol. 26, no. 4, pp. 531–550, Jul. 2007, doi: 10.1016/j.euromechflu.2006.10.003.

[78] C. G. Speziale, G. Erlebacher, T. A. Zang, and M. Y. Hussaini, “The subgrid-scale modeling of compressible turbulence,” *Phys. Fluids*, vol. 31, no. 4, p. 940, 1988, doi: 10.1063/1.866778.

[79] M. H. Silvis, R. A. Remmerswaal, and R. Verstappen, “Physical consistency of subgrid-scale models for large-eddy simulation of incompressible turbulent flows,” *Phys. Fluids*, vol. 29, no. 1, p. 015105, Jan. 2017, doi: 10.1063/1.4974093.

[80] S. Krajnović and L. Davidson, “A mixed one-equation subgrid model for large-eddy simulation,” *Int. J. Heat Fluid Flow*, vol. 23, no. 4, pp. 413–425, Aug. 2002, doi: 10.1016/S0142-727X(01)00153-9.

[81] Y. Fang and S. Menon, “A Two-Equation Subgrid Model for Large-Eddy Simulation of High Reynolds Number Flows,” Jan. 2006, doi: 10.2514/6.2006-116.

[82] F. Gallerano, E. Pasero, and G. Cannata, “A dynamic two-equation Sub Grid Scale model,” *Contin. Mech. Thermodyn.*, vol. 17, no. 2, pp. 101–123, May 2005, doi: 10.1007/s00161-004-0190-4.

[83] J. FERZIGER and D. LESLIE, “Large eddy simulation - A predictive approach to turbulent flow computation,” Jul. 1979, doi: 10.2514/6.1979-1471.

[84] J. Boussinesq, “Essai sur la théorie des eaux courantes,” *Impr. Natl.*, 1877.

[85] W. Rozema, H. J. Bae, P. Moin, and R. Verstappen, “Minimum-dissipation models for large-eddy simulation,” *Phys. Fluids*, vol. 27, no. 8, p. 085107, Aug. 2015, doi:

10.1063/1.4928700.

[86] M. Abkar, H. J. Bae, and P. Moin, “Minimum-dissipation scalar transport model for large-eddy simulation of turbulent flows,” *Phys. Rev. Fluids*, vol. 1, no. 4, p. 041701, Aug. 2016, doi: 10.1103/PhysRevFluids.1.041701.

[87] H. Lu and F. Porté-Agel, “A modulated gradient model for large-eddy simulation: Application to a neutral atmospheric boundary layer,” *Phys. Fluids*, vol. 22, no. 1, p. 015109, Jan. 2010, doi: 10.1063/1.3291073.

[88] J. BARDINA, J. FERZIGER, and W. REYNOLDS, “Improved subgrid-scale models for large-eddy simulation,” Jul. 1980, doi: 10.2514/6.1980-1357.

[89] R. AKHAVAN, A. ANSARI, S. KANG, and N. MANGIAVACCHI, “Subgrid-scale interactions in a numerically simulated planar turbulent jet and implications for modelling,” *J. Fluid Mech.*, vol. 408, pp. 83–120, Apr. 2000, doi: 10.1017/S0022112099007582.

[90] C. Meneveau and J. Katz, “Conditional subgrid force and dissipation in locally isotropic and rapidly strained turbulence,” *Phys. Fluids*, vol. 11, no. 8, pp. 2317–2329, Aug. 1999, doi: 10.1063/1.870094.

[91] J. M. Avellaneda, F. Bataille, and A. Toutant, “DNS of turbulent low Mach channel flow under asymmetric high temperature gradient: Effect of thermal boundary condition on turbulence statistics,” *Int. J. Heat Fluid Flow*, vol. 77, pp. 40–47, Jun. 2019, doi: 10.1016/j.ijheatfluidflow.2019.03.002.

[92] D. Dupuy, A. Toutant, and F. Bataille, “A posteriori tests of subgrid-scale models in strongly anisothermal turbulent flows,” *Phys. Fluids*, vol. 31, no. 6, p. 065113, Jun. 2019, doi: 10.1063/1.5098389.

[93] A. Toutant, “Numerical simulations of unsteady viscous incompressible flows using general pressure equation,” *J. Comput. Phys.*, vol. 374, pp. 822–842, Dec. 2018, doi: 10.1016/j.jcp.2018.07.058.

[94] D. Dupuy, A. Toutant, and F. Bataille, “A posteriori tests of subgrid-scale models in an isothermal turbulent channel flow,” *Phys. Fluids*, vol. 31, no. 4, p. 045105, Apr. 2019, doi: 10.1063/1.5091829.

[95] F. Aulery, D. Dupuy, A. Toutant, F. Bataille, and Y. Zhou, “Spectral analysis of turbulence in anisothermal channel flows,” *Comput. Fluids*, vol. 151, pp. 115–131, Jun. 2017, doi: 10.1016/j.compfluid.2016.06.011.

[96] M. David, A. Toutant, and F. Bataille, “Numerical development of heat transfer correlation in asymmetrically heated turbulent channel flow,” *Int. J. Heat Mass Transf.*, vol. 164, p. 120599, Jan. 2021, doi: 10.1016/j.ijheatmasstransfer.2020.120599.

[97] M. David, A. Toutant, and F. Bataille, “Direct simulations and subgrid modeling of turbulent channel flows asymmetrically heated from both walls,” *Phys. Fluids*, vol. 33, no. 8, p. 085111, Aug. 2021, doi: 10.1063/5.0058499.

[98] M. David, A. Toutant, and F. Bataille, “Investigation of thermal large-eddy simulation approaches in a highly turbulent channel flow submitted to strong asymmetric

heating," *Phys. Fluids*, vol. 33, no. 4, p. 045104, Apr. 2021, doi: 10.1063/5.0040539.

[99] F. H. Harlow and J. E. Welch, "Numerical Calculation of Time-Dependent Viscous Incompressible Flow of Fluid with Free Surface," *Phys. Fluids*, vol. 8, no. 12, p. 2182, 1965, doi: 10.1063/1.1761178.